Heliyon 7 (2021) e08429

Contents lists available at ScienceDirect

Heliyon

journal homepage: www.cell.com/heliyon

Research article

Synthesis, spectroscopic (FT-IR, FT-Raman, NMR & UV-Vis), reactive (ELF, LOL, Fukui), drug likeness and molecular docking insights on novel 4-[3-(3-methoxy-phenyl)-3-oxo-propenyl]-benzonitrile by experimental and computational methods

Shivaraj B. Radder [a,f], Raveendra Melavanki [a,f], Sudhir M. Hiremath [b,*], Raviraj. Kusanur [c], Seema S. Khemalapure [d], S. Christopher Jeyaseelan [e]

[a] Department of Physics, M S Ramaiah Institute of Technology, Bangalore, 560054, Karnataka, India
[b] Department of P.G. Studies in Physics, KLE Society's J.T. College, Gadag, 582101, Karnataka, India
[c] Department of Chemistry, R.V. College of Engineering, Bangalore, 560059, Karnataka, India
[d] P.G. Department of Studies and Research in Physics, KLE Society's P.C. Jabin Science College, Hubballi, 580031, Karnataka, India
[e] Department of Physics NMSSVN College, Nagamalai, Madurai, 19, T.N, India
[f] Affiliated to Visvesvaraya Technological University, Belgaum, 590018, Karnataka, India

ARTICLE INFO

Keywords:
DFT
FMO
NBO
NLO
NMR
UV-Vis

ABSTRACT

The spectroscopic analysis such as FT-IR, FT-Raman, UV-Vis and NMR are conducted for the synthesized molecule by both experimental and theoretical approach. The theoretical computations were achieved by DFT method with B3LYP functional and 6–311 ++ G (d, P) basis set. Firstly the geometrical parameters obtained by DFT are compared with the related experimental parameters. Experimental FT-IR and FT-Raman spectra of the title molecule have been acquired. The vibrational analysis is conducted and the assignments concerned to the observed bands are mentioned through the potential energy distribution (PED). The GIAO method was employed for theoretical NMR analysis and the results are compared with experimental chemical shifts. In accumulation to these analyses NLO, NBO, FMO and MEP analysis have been conducted to understand the nature of the molecule. ELF and LOL were performed. The drug likeness and molecular docking studies also conducted. The potency of inhibition of molecule against M^{PRO} and PL^{PRO} receptors has been performed using molecular docking studies.

1. Introduction

Nonlinear optical materials have gained huge consideration of the scientist and engineers due to their enormous applications in the field of photonics and optoelectronics [1, 2, 3, 4, 5]. Among all the organic NLO materials, chalcones exhibit outstanding NLO properties [6, 7]. Chalcones also display the photochemical and photo physical properties because of their donor-π-acceptor moieties. Chalcone derivatives contain two phenyl rings connected by ethylenic bridge of conjugated double bond. NLO properties can be improved by adding appropriate electron acceptor and electron donor groups at the different end of the ethylenic bridge. Besides the NLO properties chalcones also exhibit certain biological properties such as anticancer [8], antiviral, antiulcer, bactericidal [9], Fungicidal [10], anti malarial [11] and antitumor [12].

The above said features have enlightened us to perform the research work on the chalcone molecules. Hence in this study we have started our research work from synthesis of the on 4-[3-(3-methoxy-phenyl)-3-oxo-propenyl]-benzonitrile (4MPPB) molecule and conducted several analysis. According to conducted literature review up to here know one have conducted the experimental and computational spectral, nonlinear optical and electronic studies on the selected compound. For this reason in the present work we have concentrated on several experimental and computational studies. The experimental FT-IR, FT-Raman, UV-Vis and NMR spectral studies have been conducted at the same time the quantum computational studies have been performed by Gaussian software. The detailed vibrational (FT-IR, FT-Raman) analysis have been conducted and complete vibrational assignments have been established by VEDA 04 software. The NMR (^{1}H and ^{13}C) chemical shift values have been established by experimental and computational method. The HOMO-

* Corresponding author.
E-mail address: sudheerh24@gmail.com (S.M. Hiremath).

https://doi.org/10.1016/j.heliyon.2021.e08429
Received 16 September 2021; Received in revised form 21 October 2021; Accepted 16 November 2021

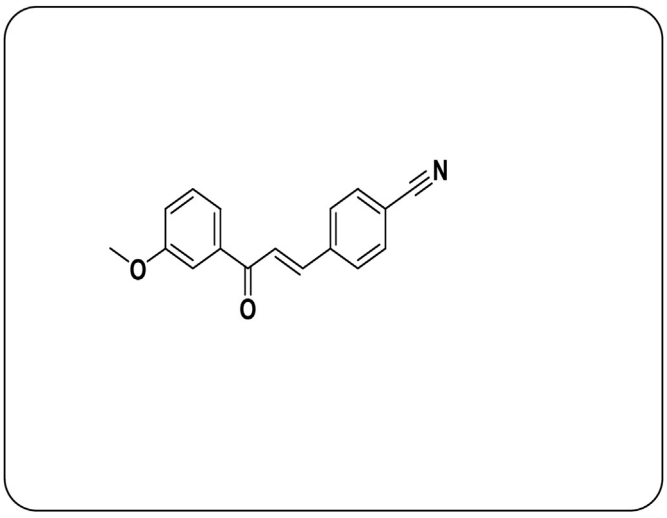

Figure 1. Synthesised structure of 4MPPB.

LUMO analysis is helpful to determine the charge transfer properties of the selected molecule. MEP surface analysis has been found on optimized structure of the title molecule. Electron localization function (ELF) and localized orbital locator (LOL) analysis have helpful to determine the regions of bond pairs, lone pairs and size of the bonding the molecule. Along with these properties Fukui function, drug likeness and molecular docking studies have been performed.

2. Materials and methods

2.1. Material

The synthesis of -[3-(3-Methoxy-phenyl)-3-oxo-propenyl]-benzonitrile (4MPPB) molecule have been performed by the following process as per the literature [13, 14]. Equimolar quantities of 3-methoxy acetophenone and 4-cyanobenzaldehyde are dissolved in ethanol 20 ml aqueous sodium hydroxide solution 2ml (40%) is added dropwise with stirring for 10 min. The stirring is continued at room temperature for 5 h. TLC (5% ethyl acetate in hexane) is confirmed the completion of the reaction. The reaction quenched in ice, solid separated is filtered and dried. Purified by recrystallisation in 10% ethyl acetate and hexane mixture to give yellow-coloured crystals. The NMR and IR spectral data of the selected molecule have been helpful to determine the molecular structural properties and structure is mentioned in Figure 1.

2.2. Experimental methods

The PerkinElmer spectrometer is used to obtain the FT-IR spectrum at room temperature in the range 4000-400 cm^{-1} along with the 100 number of scans and 2.0 cm^{-1} resolution. The UV-Visible spectrometer (Model: Agilent Technology's Cary series) is used to obtain the absorption spectra of the title molecule in the region 900-100 nm. FT-Raman spectrum is measured in the range 4000-100 cm^{-1} with the help of BRUKER RFS 27: stand-alone FT-Raman spectrometer model. The signals measured at room temperature along with the 100 scan numbers and 2 cm^{-1} resolution. ^{1}H and ^{13}C NMR spectra are measured at 500 MHz in DMSO-d_6 with the help of JNM-ECZ4005 FT-NMR spectrometer model, TMS taken as the standard reference. The chemical shifts are expressed in δ ppm.

2.3. Computational methods

The complete theoretical computations achieved with the help of DFT method with B3LYP functional and 6–311 ++ G (d, P) basis set available in Gaussian 09w software [15]. Gauss View 5.0 [16] is utilized to visualize the molecule. The complete optimization of the structure is carried out. The optimization process provides the minimum energy confirmation of the structure. The computation of theoretical and experimental wave numbers is achieved at same basis level. Generally computed vibrational wavenumbers are found to be greater than the experimentally obtained wavenumbers. Hence to obtain proper comparison between experimental and theoretical wave numbers, the theoretical wavenumbers are scaled by the scaling factor of 0.9614 [17]. The entire

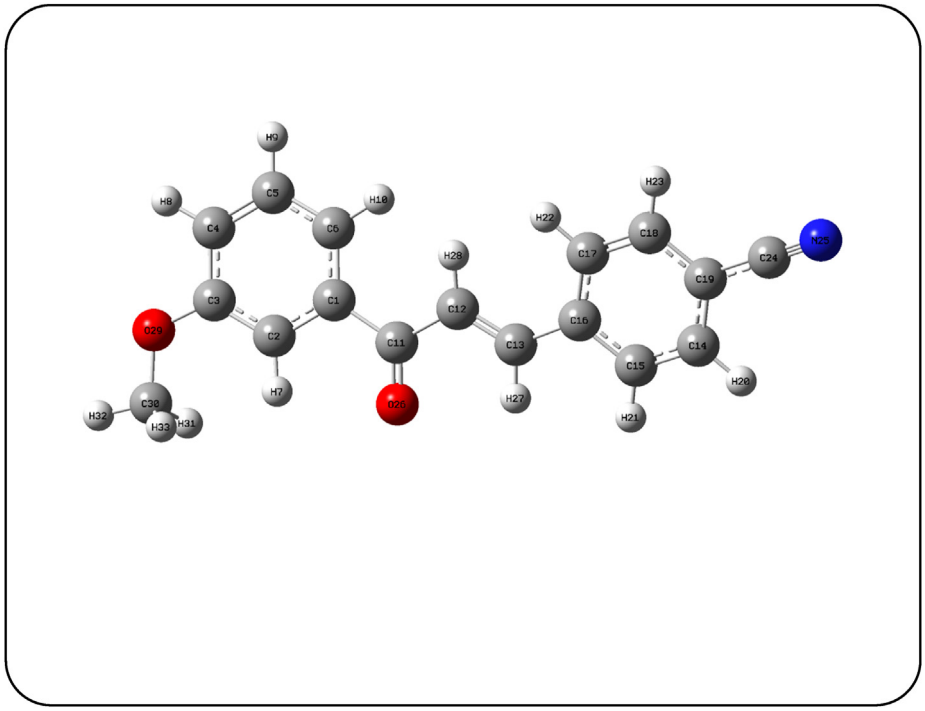

Figure 2. Optimized geometric structure with atoms numbering of 4MPPB.

Table 1. Geometrical parameters of 4MPPB by X-ray (Taken from Ref [21]) and DFT.

Parameter	DFT	XRD
Bond lengths (Å)		
C1–C2	1.54	1.40
C1–C6	1.36	1.39
C1–C11	1.54	1.48
C2–C3	1.36	1.37
C2–H7	1.07	0.93
C3–C4	1.54	1.41
C3–O29	1.43	1.36
C4–C5	1.36	1.38
C4–H8	1.07	
C5–C6	1.54	1.38
C5–H9	1.07	0.93
C6–H10	1.07	0.93
C11–C12	1.54	1.48
C11–O26	1.26	1.22
C12–C13	1.36	1.32
C12–H28	1.07	0.93
C13–C16	1.54	1.47
C13–H27	1.07	0.93
C14–C15	1.36	1.39
C14–C19	1.54	1.36
C14–H20	1.07	0.93
C15–C16	1.54	1.39
C15–H21	1.07	0.93
C16–C17	1.36	1.39
C17–C18	1.54	1.38
C17–H22	1.07	0.93
C18–C19	1.36	1.37
C18–H23	1.07	0.93
C19–C24	1.54	
C24–N25	1.15	
O29–C30	1.43	1.42
C30–H31	1.07	0.96
C30–H32	1.07	0.96
C30–H33	1.07	0.96
Bond angles (°)		
C2–C1–C6	120.00	121.50
C2–C1–C11	120.00	117.40
C6–C1–C11	120.00	124.30
C1–C2–C3	120.00	121.50
C1–C2–H7	120.00	119.20
C3–C2–H7	120.00	119.20
C2–C3–C4	120.00	119.60
C2–C3–O29	120.00	125.10
C4–C3–O29	120.00	115.30
C3–C4–C5	120.00	119.20
C3–C4–H8	120.00	
C5–C4–H8	120.00	
C4–C5–C6	120.00	120.50
C4–C5–H9	120.00	119.80
C6–C5–H9	120.00	119.70
C1–C6–C5	120.00	120.90
C1–C6–H10	120.00	119.50
C5–C6–H10	120.00	119.60
C1–C11–C12	120.00	119.60
C1–C11–O26	120.00	120.20
C12–C11–O26	120.00	120.20
C11–C12–C13	120.00	121.20
C11–C12–H28	120.00	119.40
C13–C12–H28	120.00	119.40
C12–C13–C16	120.00	127.40
C12–C13–H27	120.00	116.30
C16–C13–H27	120.00	116.30
C15-14-C19	120.00	118.90
C15–C14–H20	120.00	120.60
C19–C14–H20	120.00	120.50
C14–C15–C16	120.00	120.90
C14–C15–H21	120.00	119.50
C16–C15–H21	120.00	119.50
C13–C16–C15	120.00	119.10
C13–C16–C17	120.00	123.10
C15–C16–C17	120.00	119.10
C16–C17–C18	120.00	121.60
C16–C17–H22	120.00	119.20
C18–C17–H22	120.00	119.20
C17–C18–C19	120.00	118.20
C17–C18–H23	120.00	120.90
C19–C18–H23	120.00	120.90
C14–C19–C18	120.00	122.60
C14–C19–C24	120.00	
C18–C19–C24	120.00	
C3–O29–C30	109.47	117.30
O29–C30–H31	83.95	109.50
O29–C30–H32	140.09	109.50
O29–C30–H33	82.58	109.50
H31–C30–H32	84.36	109.40
H31–C30–H33	139.36	109.50
H32–C30–H33	81.92	109.50
Dihedral angles (°)		
C6–C1–C2–C3	0.00	1.40
C6–C1–C2–H7	-180.00	-178.50
C11–C1–C2–C3	-180.00	-175.90
C11–C1–C2–H7	0.00	4.20
C2–C1–C6–C5	0.00	-1.10
C2–C1–C6–H10	-180.00	178.90
C11–C1–C6–C5	-180.00	176.00
C11–C1–C6–H10	0.00	-4.00
C2–C1–C11–C12	180.00	179.40
C2–C1–C11–O26	0.00	-0.20
C6–C1–C11–C12	0.00	2.30
C6–C1–C11–O26	180.00	-177.30
C1–C2–C3–C4	0.00	-0.40
C1–C2–C3–O29	180.00	179.70
H7–C2–C3–C4	180.00	179.60
H7–C2–C3–O29	0.00	-0.30
C2–C3–C4–C5	0.00	-1.00
C2–C3–C4–H8	-180.00	
O29–C3–C4–C5	-180.00	178.90
O29–C3–C4–H8	0.00	
C3–C4–C5–C6	0.00	1.40
C3–C4–C5–H9	180.00	-178.60
H8–C4–C5–C6	180.00	
H8–C4–C5–H9	0.00	
C4–C5–C6–C1	0.00	-0.30
C4–C5–C6–H10	180.00	179.70
H9–C5–C6–C1	-180.00	179.60

(*continued on next page*)

Table 1 (*continued*)

Parameter	DFT	XRD
Bond lengths (Å)		
H9–C5–C6–H10	0.00	-0.40
C1–C11–C12–C13	180.00	-163.20
C1–C11–C12–H28	0.00	16.80
O26–C11–C12–C13	0.00	16.40
O26–C11–C12–H28	180.00	-163.60
C11–C12–C13–C16	-180.00	-178.50
C11–C12–C13–H27	0.00	1.50
H28–C12–C13–C16	0.00	1.50
H28–C12–C13–H27	-180.00	-178.50
C12–C13–C16–C15	180.00	-176.70
C12–C13–C16–C17	0.00	4.00
H27–C13–C16–C15	0.00	3.30
H27–C13–C16–C17	180.00	-176.00
C19–C14–C15–C16	0.00	0.40
C19–C14–C15–H21	180.00	-179.60
H20–C14–C15–C16	180.00	-179.60
H20–C14–C15–H21	0.00	0.40
C15–C14–C19–C18	0.00	-0.60
C15–C14–C19–C24	-180.00	
H20–C14–C19–C18	-180.00	179.40
H20–C14–C19–C24	0.00	
C14–C15–C16–C13	-180.00	-179.10
C14–C15–C16–C17	0.00	0.30
H21–C15–C16–C13	0.00	0.90
H21–C15–C16–C17	-180.00	-179.70
C13–C16–C17–C18	180.00	178.50
C13–C16–C17–H22	0.00	-1.60
C15–C16–C17–C18	0.00	-0.90
C15–C16–C17–H22	180.00	179.10
C16–C17–C18–C19	0.00	0.80
C16–C17–C18–H23	-180.00	-179.20
H22–C17–C18–C19	-180.00	-179.20
H22–C17–C18–H23	0.00	0.80
C17–C18–C19–C14	0.00	0.00
C17–C18–C19–C24	180.00	
H23–C18–C19–C14	180.00	180.00
H23–C18–C19–C24	0.00	
C3–O29–C30–H31	-68.25	-59.90
C3–O29–C30–H32	-141.95	60.20
C3–O29–C30–H33	150.19	-179.80

vibrational assignments for the computed wave numbers of the title molecule is conducted with the help of PED (%) acquired by VEDA 04 software [18]. The NMR (^{1}H, ^{13}C NMR) chemical shift values are acquired with help of GIAO method with the same basis level. The TD-DFT method [19] is used to estimate the theoretical UV-Vis spectral parameters at same basis level. The NBO, HOMO-LUMO, MEP and NLO properties have been obtained by optimized structure with the help of suitable methods in the Gaussian tool. Multiwfn software is employed to conduct the Fukui function analysis [20].

3. Results and discussion

3.1. Molecular geometry

Optimized molecular geometrical structure with numbering of atoms and the geometrical parameters like bond angle, bond length and dihedral angles of the present molecule is obtained from DFT method with B3LYP functional and 6–311 ++ G (d, P) basis set and 3D picture presented in Figure 2. The experimental geometrical parameters of the title molecule are not available. So for comparison study, we have taken the experimental geometrical parameters of the similar reported molecules. The bond angles, bond lengths and dihedral angles obtained by theoretical computation are compared with the reported XRD data [21]. Both the experimental as well as geometrical parameters are mentioned in Table 1. There is small variation in the theoretical and experimental results because the experimental part has been performed in the solid phase and theoretical calculation has been conducted in the gas phase [22].

The 4MPPB is made up of 34 bonds; they are seventeen C–C, thirteen C–H, three C–O bonds and one C≡N bond. In the title molecule the bond length of the C11 = O26 in the ethylenic bridge is 1.258 Å in DFT and 1.224 Å in XRD. The C–C bond length in the title molecule lies in the range of 1.355-.1.54Å. The ethylenic group act as the bridge between phenyl ring and benzonitrile, so the bond lengths and dihedral angle of this ethylene bridge become important. The C–C–C, C–C–O bond angle in ethylenic bridge are C11–C12–C13 (120/121.2), C1–C11–C12 (119.99/119.6), C12–C13–C16 (119.99/127.4), C1–C11–O26 (120/120.2), C12–C11–O26 (120/120.2). The important dihedral angle (DFT/XRD) in ethylenic bridge are C1–C11–C12–C13 is 179.9987/-163.2,C11–C12–C13–C16 is -180/-178.5. All the bond length, bond angle and dihedral angles are presented in Table 1.

3.2. Vibrational assignment

The synthesized 4MPPB has been characterized by FT-IR, FT-Raman analysis; the spectra obtained by experimental techniques are compared with computational spectra. The 4MPPB is consists of 33 atoms having 99 fundamental vibrational modes. The experimental and theoretical spectra of FT-IR, FT-Raman analysis are displayed in figures.3 and 4. Theoretically computed wavenumbers (scaled and unscaled), experimentally obtained FT-Raman and FT-IR wavenumbers, detailed vibrational assignments (PED %) are mentioned in Table 2. There is small discrepancy in the theoretical and experimental results because the experimental part taken in the solid phase and theoretical calculation conducted in the gas phase.

3.2.1. Ethylenic bridge

The carbonyl structure in ethylenic bridge acts as prominent role in the process of charge transfer. C=O stretching in experimental spectra can be easily identified due to its higher strength, degree of conjugation and better polarization nature [23]. C=O is formed due to the conjugation of π bond among carbon and oxygen. The uneven sharing of bonding electrons occurs because of the difference in electro negativity's of the carbon atom and oxygen atom. The occurrence of the lone pair of electrons on the oxygen atom is accountable the polar nature of carbonyl group. According to the previous studies elevated peaks indicating C=O stretching are observed in the IR around 1600-1850 cm^{-1} [24].

In the present study, stretching of C=O appeared at 1655 cm^{-1} in FT-Raman and occurred as strong band at 1648 cm^{-1} in IR. The computational peak found at 1652 cm^{-1}. The C11 = C12 stretching is appeared as strong peak at 1601 cm^{-1}in Raman and 1595 cm^{-1} in IR. The computational peak found at 1587 cm^{-1}. The C–H stretching is occurred at 3040 cm^{-1} and DFT peak found at 3029 cm^{-1}. The C–H in plane bending commonly occur around 1300-1000 cm^{-1} [25]. In 4MPPB, CH in-plane bending are theoretically computed at 1303, 1298 cm^{-1} and corresponding Raman peak found at 1289 cm^{-1}. The peaks C–H out of plane bending mode identified at 981cm^{-1} in FT-IR and is matched with the DFT wave number at 984 cm^{-1}.

3.2.2. Phenyl ring 1

The C–H stretching concerned to the phenyl ring takes place in the span of 3010–3120 cm^{-1} [26-27]. In title molecule, the stretching of C–H vibrations are computed at 3096, 3089, 3073, 3069, 3051 cm^{-1}, the IR peaks recognized at 3070 cm^{-1}. The C–H in plane bending vibrations

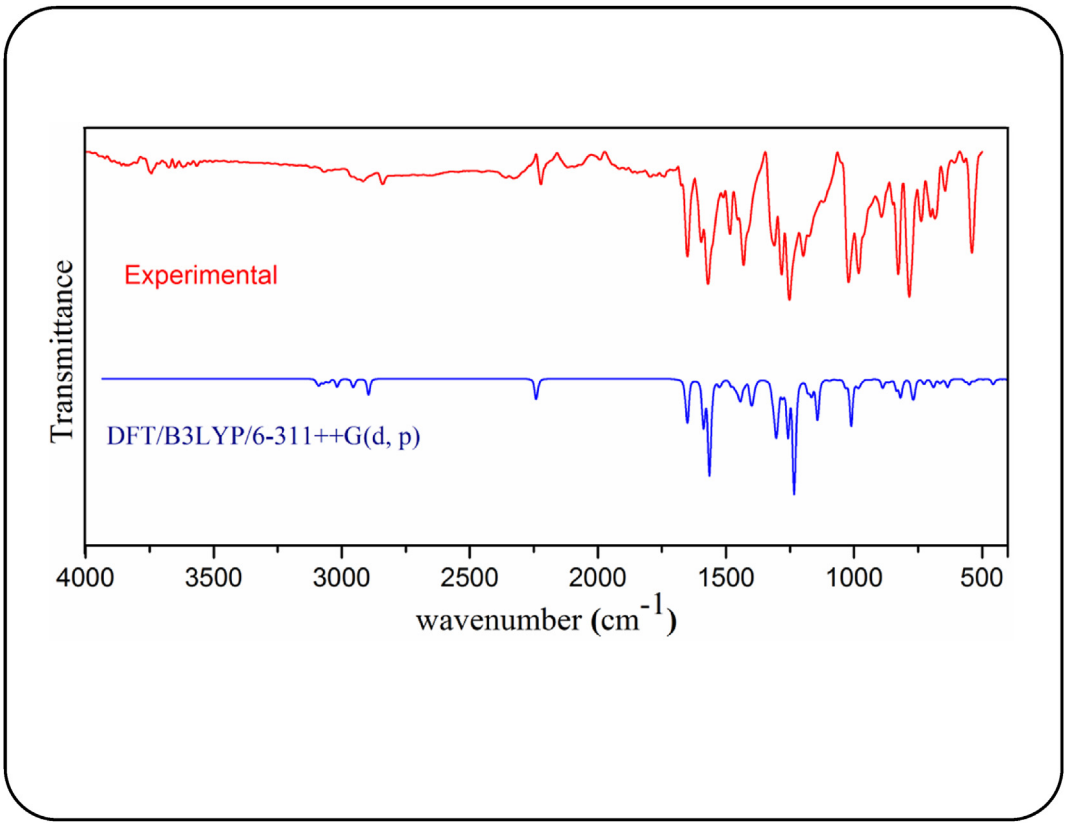

Figure 3. Experimental and simulated FT-IR spectra of 4MPPB.

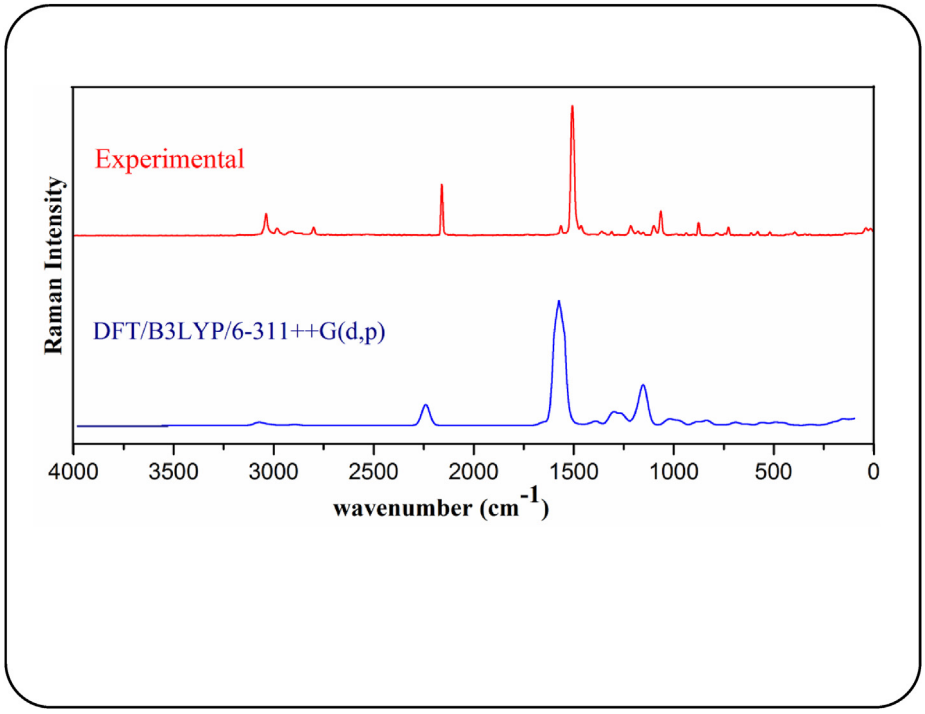

Figure 4. Experimental and simulated FT-Raman spectra of 4MPPB.

marginally merged along C–C stretching vibrations are appear in the span of 1500-1000 cm^{-1} [28]. The C–H in plane bending peaks obtained at 1454, 1312, 1022 cm^{-1} in IR and 1460, 1410, 1321, 1264, 1053 cm^{-1} Raman, the hypothetical peaks observed at 1461, 1400, 1315, 1262, 1141, 1063, 1032 cm^{-1}. The out of plane C–H bendings commonly predicted in the span of 1000-675 cm^{-1} [29]. The out of plane C–H bendings computed at 948, 881, 868, 771, 727 cm^{-1}, the FT-IR and FT-Raman bands found at 783, 736 and 867 cm^{-1} respectively. The breathing mode in ring is observed at 970 cm^{-1} in DFT. The phenyl ring undergoing torsion is observed at cm^{-1} 409, 530 cm^{-1}in FT-Raman, 539

Table 2. Detailed assignments of experimental and theoretical wave numbers of 4MPPB with 6–311++G (d, p) basis set.

Modes	Experimental wavenumber		Theoretical wavenumber				Assignments with PED (≥10%)
	FT-IR	FT-Raman	B3LYP unscaled	B3LYP scaled	I^{IR}	S^a	
93	-	-	3220	3096	8.6047	47.4955	ν(C2–H7) (99)
92	-	-	3213	3089	13.7733	97.1245	ν(C6–H10) (56),ν(C12–H28) (37)
91	-	3077 ms	3201	3077	0.7026	72.5263	ν(C17–H22) (32),ν(C18–H23) (46)
90	-	-	3199	3075	3.2535	144.0192	ν(C14–H20) (81),ν(C15–H21) (11)
89	-	-	3197	3073	4.4628	147.3629	ν(C4–H8) (39),ν(C5–H9) (14),ν(C12–H28) (26),ν(C18–H23) (14)
88	3070 vw	-	3193	3069	5.3318	102.1866	ν(C4–H8) (44),ν(C6–H10) (23),ν(C12–H28) (24)
87	-	-	3184	3061	2.6989	20.0804	ν(C17–H22) (62),ν(C18–H23) (30)
86	-	-	3177	3054	3.3331	50.6895	ν(C14–H20) (12),ν(C15–H21) (87)
85	-	-	3174	3051	7.541	85.3187	ν(C4–H8) (14),ν(C5–H9) (78)
84	3040 vw	-	3151	3029	0.3548	29.1694	ν(C13–H27) (98)
83	3011 w	3020 w	3138	3017	24.833	176.812	ν_{asym} (CH_3) (91)
82	2917 w	2954 vw	3073	2954	31.3761	43.2945	ν_{asym} (CH_3) (98)
81	2840 w	2845 w	3012	2895	43.6096	160.923	ν_{sym} (CH_3) (91)
80	2222 w	2230 s	2330	2240	66.1368	1812.584	ν(N25–C24) (89),ν(C19–C24) (11)
79	1648 s	1655 w	1718	1652	144.7216	155.169	ν(O26–C11) (57),ν(C12–C13) (20)
78	1595 s	1601 vs	1651	1587	127.5097	307.8876	ν(O26–C11) (12),ν(C12–C13) (20),ν(C17–C18) (13)
77	-	-	1641	1577	11.2544	5977.712	ν(C12–C13) (12),ν(C17–C18) (18))
76	1568 vs	-	1626	1563	295.3045	2530.055	ν(O26–C11) (15),ν(C4–C5) (12),ν(C2–C3) (10),ν(C1–C2)14)
75	-	1561 w	1623	1560	4.4711	526.9961	ν(C3–C4) (26),β(C4–C5–C6) (16)
74	1511 vw	-	1585	1524	24.317	231.256	ν(C14–C19) (25),ν(C15–C16) (21)
73	1485 ms	-	1537	1478	22.0895	43.6817	β(H20–C14–C15) (16),β(H21–C15–C14) (18), β(H22–C17–C18) (15),β(H23–C18–C17) (16)
72	1454 ms	1460 vw	1520	1461	33.9723	1.6229	β(H7–C2–C1) (12),β(H9–C5–C6) (26),β(H31–C30–H33) (11)
71	-	-	1503	1445	77.2819	5.3039	β_{asym} (CH_3) (91)
70	1430 s	-	1493	1436	10.1068	14.5821	β_{asym} (CH_3) (97)
69	-	-	1483	1426	10.0879	20.7665	β_{sym} (CH_3) (72)
68	-	1410 vw	1456	1400	104.9845	42.7728	ν(C2–C3) (10),ν(C1–C2) (14),β(H8–C4–C5) (12), β(H10–C6–C1) (11),γ(C30–H31–O29–H33) (12)
67	-	-	1441	1385	14.2101	103.3619	ν(C17–C18) (23),ν(C14–C15) (22),β(H20–C14–C15) (10), β(H22–C17–C18) (10)
66	1312 s	1321 w	1367	1315	87.2703	145.6859	ν(C4–C5) (27),ν(C1–C2) (17)
65	-	-	1355	1303	106.7004	96.7893	β(H27–C13–C12) (34),β(H20–C14–C15) (10)
64	-	1289 vw	1350	1298	61.3795	160.7505	ν(C12–C13) (11),β(H28–C12–C13) (45)
63	1283 s	-	1330	1278	43.9422	13.4793	ν(C14–C19) (13),β(H27–C13–C12) (10), β(H21–C15–C14) (10),β(H22–C17–C18) (16),β(H23–C18–C17) (14)
62	-	1264 vw	1312	1262	19.4434	157.0654	β(H7–C2–C1) (20),β(H9–C5–C6) (13),β(H10–C6–C1) (14)
61	1253 vs	-	1308	1258	133.1824	125	ν(C15–C16) (10),ν(C18–C19) (12),ν(C13–C16) (10)
60	-	-	1282	1233	354.6277	42.9982	ν(O29–C3) (33)
59	1199 s	-	1235	1187	1.7516	169	ν(C17–C18) (19),ν(C14–C15) (11),ν(C13–C16) (13), β(H27–C13–C12) (10),β(H22–C17–C18) (10)
58	1177 ms	-	1227	1180	28.6016	42	ν(C19–C24) (19),β(H21–C15–C14) (20)
57	-	1174 ms	1214	1167	46.5069	21	$\delta_{out\ of\ plane}$ (CH_3) (65)
56	-	-	1199	1153	1.6901	747	β(H20–C14–C15) (19),β(H21–C15–C14) (11),β(H23–C18–C17) (15)
55	-	-	1191	1145	64.8019	97	β(H8–C4–C5) (12),β(H9–C5–C6) (19),β(H32–C30–O29) (13)

(*continued on next page*)

Table 2 (*continued*)

Modes	Experimental wavenumber		Theoretical wavenumber				Assignments with PED (≥10%)
	FT-IR	FT-Raman	B3LYP unscaled	B3LYP scaled	I^{IR}	S^a	
54	-	-	1187	1141	62.0445	112.5933	β(H7–C2–C1) (12),β(H9–C5–C6) (14),β(H10–C6–C1) (21)
53	1118 w	-	1168	1123	0.6538	2.3331	$\delta_{in\ plane}$ (CH_3) (80)
52	-	-	1138	1094	4.6425	9.4374	ν(C17–C18) (10),ν(C14–C15) (18),β(H20–C14–C15) (17), β(H21–C15–C14) (11),β(H22–C17–C18) (15),β(H23–C18–C17) (14)
51	-	1053 vw	1106	1063	2.0945	1.7398	ν(C4–C5) (15),ν(C5–C6) (29),β(H8–C4–C5) (28)
50	1022 vs	-	1074	1032	24.9272	83.0071	ν(C11–C12) (18),ν(O29–C30) (10),β(H7–C2–C1) (15)
49	-	1017 w	1051	1011	129.6362	62.357	ν(C11–C12) (13),ν(O29–C30) (59)
48	-	993 ms	1033	993	1.9975	7.0339	β(C17–C18–C19) (46),β(C15–C14–C19) (30),β(C14–C19–C18) (19)
47	981 s	-	1023	984	28.9288	15.2745	τ(H28–C12–C13–C16) (10),τ(H27–C13–C16–C15) (76)
46	-	-	1009	970	8.2727	67.6567	ν(C3–C4) (17),β(C3–C4–C5) (11),β(C4–C5–C6) (25), β(C2–C3–C4) (21)
45	-	-	988	950	0.0454	0.1505	τ(H20–C14–C19–C24) (26),γ(C15–C14–C16–H21) (30), γ(C17–C16–C18–H22) (18),τ(H23–C18–C19–H24) (19)
44	-	-	986	948	0.0609	0.7039	γ(C4–C3–C5–H8) (10),τ(H8–C4–C5–H9) (77)
43	-	-	976	938	3.1999	1.0611	τ(H20–C14–C19–C24) (18),γ(C15–C14–C16–H21) (15), γ(C17–C16–C18–H22) (22),τ(H23–C18–C19–H24) (28)
42	894 ms	-	925	889	23.0105	45.2102	ν(C11–C12) (17),β(C11–C12–C13) (13),β(C12–C13–C16) (11)
41	-	-	916	881	2.8944	9.927	τ(H7–C2–C3–C4) (41),τ(H28–C12–C13–C16) (14)
40	-	867 vw	903	868	7.8366	0.2369	γ(C4–C3–C5–H8) (43),τ(H10–C6–C1–C2) (34)
39	-	849 w	895	860	5.3325	7.0893	τ(H7–C2–C3–C4) (20),τ(H28–C12–C13–C16) (47)
38	849 ms	830 vw	867	834	28.5889	71.9506	β(C14–C19–C18) (18)
37	828 s	-	851	818	45.1784	2.3376	τ(H20–C14–C19–C24) (32),γ(C15–C14–C16–H21) (32)
36	-	811 vw	845	812	6.663	0.0778	γ(C17–C16–C18–H22) (43),τ(H23–C18–C19–C24) (39)
35	783vs	-	802	771	33.062	3.8629	γ(C4–C3–C5–H8) (25),τ(H10–C6–C1–C2) (14), τ(C1–C6–C5–C4) (11),τ(C3–C4–C5–C6) (12)
34	-	-	799	768	46.5276	2.8832	ν(C14–C19) (10),ν(C18–C19) (11),β(C1–C11–O26) (10)
33	736 ms	-	756	727	13.2282	4.8338	τ(H10–C6–C1–C2) (11),τ(C16–C17–C18–C19) (19), τ(C16–C15–C14–C19) (20),γ(O26–C1–C12–C11) (20)
32	700 ms	-	719	691	25.7869	31.4713	ν(C19–C24) (14),β(C14–C15–C16) (16)
31	685 ms	-	714	687	4.9249	4.0873	τ(H10–C6–C1–C2) (10),τ(C16–C17–C18–C19) (15), τ(C16–C15–C14–C19) (15),γ(O26–C1–C12–C11) (20)
30	-	-	690	663	13.6472	0.383	τ(H7–C2–C3–C4) (13),τ(H10–C6–C1–C2) (11), τ(C2–C3–C4–C5) (29),τ(C1–C6–C5–C4) (21)
29	645 w	-	664	638	8.5712	10.4341	β(C14–C15–C16) (16),β(C15–C14–C19) (18)
28	608 vw	-	659	633	18.0973	4.3737	β(C1–C11–O26) (15),β(C3–C4–C5) (19)
27	571 vw	568 vw	585	563	9.4812	18.0052	β(C4–C5–C6) (11),β(C1–C11–C12) (12),β(C3–O29–C30) (10)

(*continued on next page*)

Table 2 (*continued*)

Modes	Experimental wavenumber		Theoretical wavenumber				Assignments with PED (≥10%)
	FT-IR	FT-Raman	B3LYP unscaled	B3LYP scaled	I^{IR}	S^a	
26	-	552 vw	572	550	10.8447	3.693	β(C19–C24–N25) (15),τ(C14–C19–C24–N25) (17), τ(C15–C14–C19–C18) (12),τ(C15–C14–C19–C24) (18)
25	-	-	570	548	4.1883	5.5499	β(C19–C24–N25) (24),β(C14–C19–C24) (22), τ(C14–C19–C24–N25) (13)
24	539 *s*	530 w	552	530	8.3195	1.1162	τ(C1–C6–C5–C4) (24),γ(O26–C1–C12–C11) (10), τ(C5–C4–C3–O29) (15)
23	-	482 vw	517	497	1.7041	20.3067	β(C12–C13–C16) (19),β(C1–C11–C12) (18)
22	-	458vw	477	458	14	11.4766	ν(C19–C24) (10),β(C1–C11–O26) (21)
21	-	-	468	450	3	2.1128	τ(C14–C19–C24–N25) (16),τ(C13–C16–C15–C14) (17), τ(C15–C14–C19–C18) (35)
20	-	-	458	440	1	3.6384	ν(O29–C3) (10),β(C2–C3–C4) (12),β(C4–C3–O29) (32), β(C3–O29–C30) (15)
19	-	409 vw	438	421	1	0.157	τ(C2–C3–C4–C5) (11),τ(C1–C6–C5–C4) (14),τ(C3–C4–C5–C6) (46)
18	-	-	413	397	5.0793	1.4136	ν(C1–C11) (18),β(C2–C1–C6) (21),β(C13–C16–C15) (14)
17	-	-	408	392	0.0431	0.0652	β(C16–C17–C18–C19) (49),β(C16–C15–C14–C19) (35)
16	-	316 vw	328	315	1.8685	3.3338	β(C2–C1–C11) (26),β(C3–O29–C30) (25)
15	-	286 w	292	281	1.8652	0.0527	τ(C14–C19–C24–N25) (17),τ(C13–C16–C15–C14) (27), τ(C15–C14–C19–C18) (16),τ(C11–C12–C13–C16) (18)
14	-	-	266	256	0.9444	0.4347	τ(H31–C30–O29–C3) (58),τ(C2–C3–C4–C5) (12), τ(C5–C4–C3–O29) (19)
13	-	-	247	237	3.1439	1.4504	β(C13–C16–C15) (15),β(C4–C3–O29) (13), β(C1–C11–C12) (13),β(C3–O29–C30) (14)
12	-	225 w	211	202	1.6906	4.6926	τ(CH3) (46)
11	-	188 w	202	194	1.221	0.4981	β(C11–C12–C13) (11),τ(C5–C4–C3–O29) (13)
10	-	165 w	166	159	0.7645	5.0236	τ(C1–C11–C12–C13) (12),τ(C3–C2–C1–C11) (46)
9	-	-	154	148	2.4301	1.6375	β(C19–C24–N25) (11),β(C14–C19–C24) (14),β(C4–C3–O29) (12)
8	-	140 w	145	140	1.2482	0.0352	τ(C14–C19–C24–N25) (12),τ(C11–C12–C13–C16) (24),τ(C15–C14–C19–C24) (37)
7	-	-	123	118	6.1941	2.6467	β(C19–C24–N27) (11),β(C14–C19–C24) (13), β(C2–C1–C11) (18)
6	-	-	95	92	2.3064	0.9486	τ(C4–C3–O29–C30) (70)
5	-	86 ms	85	82	4.5456	0.9362	τ(C1–C11–C12–C13) (16),τ(C12–C13–C16–C15) (16),τ(C11–C12–C13–C16) (11),τ(C4–C3–O29–C30) (13),τ(C3–C2–C1–C11) (13)
4	-	67 ms	54	52	4.7615	1.0696	τ(C1–C11–C12–C13) (21),τ(C13–C16–C15–C14) (32), τ(C15–C14–C19–C24) (14)
3	-	-	42	41	0.6424	2.196	β(C11–C12–C13) (25),β(C13–C16–C15) (10), β(C12–C13–C16) (27),β(C1–C11–C12) (15)
2	-	-	17	16	0.0094	1.7473	τ(C1–C11–C12–C13) (30),τ(C12–C13–C16–C15) (46), τ(C2–C1–C11–C12) (10)
1	-	-	12	11	0.0413	1.4211	τ(C12–C13–C16–C15) (14),τ(C2–C1–C11–C12) (66)

vs: very strong; s: strong; ms: medium strong; w: weak; vw: very weak [ν = stretching, β = Bending, τ = torsion, λ = out of plane bending, δ = rocking; sym = symmetric; asym = asymmetric]; I^{IR}:IR intensity; S^a:Raman activity.

Table 3. Experimental and theoretical ^{13}C and ^{1}H NMR chemical shifts [with respect to TMS, all values in ppm] of 4MPPB.

C-Atom	DFT	Experimental	H-Atom	DFT	Experimental
11-C	192.33	189.49	22-H	8.44	7.79
3-C	167.13	160.03	27-H	8.26	7.75
13-C	150.30	142.11	28-H	8.25	7.72
16-C	144.85	142.11	20-H	8.00	7.61
1-C	144.24	139.98	23-H	7.98	7.6
14-C	140.10	139.98	10-H	7.97	7.59
18-C	139.28	132.72	7-H	7.93	7.56
15-C	139.14	132.72	21-H	7.86	7.54
5-C	134.38	129.77	9-H	7.68	7.45
17-C	130.22	128.79	8-H	7.47	7.43
4-C	128.74	125.08	32-H	4.14	3.89
12-C	126.43	121.13	31-H	3.84	3.89
6-C	126.40	119.79	33-H	3.82	3.89
24-C	125.75	118.43			
19-C	117.06	113.5			
2-C	112.75	112.94			
30-C	55.38	55.55			

cm^{-1}in FT-IR, and calculated values observed at 421, 530 cm^{-1}. The other mixed with other modes and all the modes mentioned in Table 2.

3.2.3. Phenyl ring 2

In the phenyl structure the C–H stretching's are expected in the span of 3010–3120 cm^{-1} [26] IN 4MPPB, the C–H stretching vibrations in phenyl ring are recognized at 3077 cm^{-1} in Raman and computed at 3077, 3075, 3061, 3054 cm^{-1}. The C–H in plane bending vibrations marginally mixed along with C–C stretching vibrations appears in the span of 1500-1000 cm^{-1} [28]. The C–H in plane bending vibrations for 4MPPB molecule are computed at 1478, 1385, 1278, 1153, 1094 cm^{-1} and found at 1485, 1283 cm^{-1} in IR. The out of plane bending vibrations are calculated at 950, 938, 818, 812 cm^{-1} and the corresponding experimental IR values observed at 828 cm^{-1} and Raman value found at 811 cm^{-1}. The phenyl ring undergoing torsion is obtained at 552cm^{-1} in Raman and DFT values found at 450, 550 cm^{-1}. The N≡C stretching modes generally takes place in the span of 2260-2120 cm^{-1} [30]. The N≡C stretching vibration in 4MPPB theoretically computed at 2240 cm^{-1} and corresponding FT-IR and FT-Raman values obtained at 2222 cm^{-1} and 2230 cm^{-1}.

3.2.4. O–CH_3 vibrations

In the 4MPPB the methoxy group is connected to the first phenyl ring, the wave number of CH_3 stretching vibrations are reduced due to the attachment of oxygen atom [31, 32]. Generally in O–CH_3 group, the symmetric and asymmetric (CH_3) stretching vibrations found in the region of 2870-2825 cm^{-1} and 2985 ± 80 cm^{-1} respectively [31, 32]. In 4MPPB, computed wave numbers 3017 (91%), 2954 (98%) and 2895 (90%) cm^{-1} indicate the asymmetric & symmetric (CH_3) stretching modes. The Raman and IR peaks observed at 3020, 2954, 2845 and 3011, 2917, 2840 respectively. For symmetric and asymmetric bending vibrations the theoretical values observed at 1426 and 1445, 1436 cm^{-1} respectively. The IR peak for asymmetric bending is detected at 1430 cm^{-1}. The O–CH_3 stretching modes generally crop up in the region of 1100-1000 cm^{-1} [32]. In 4MPPB, O–CH_3 stretching modes computed at 1011 cm^{-1} and corresponding Raman peak observed at 1017 cm^{-1}. The bending mode of O–CH_3 is usually found to be 670-300 cm^{-1}. In 4MPPB, O–CH_3 bending modes are observed at 571 and 568 cm^{-1} in IR and Raman respectively and corresponding computed value is 563 cm^{-1}. In 4MPPB, CH_3 rocking vibrations (in-plane and out of plane) are computed at 1167 and 1123 cm^{-1}. For out of plane rocking, FT-IR peak viewed at 1118 cm^{-1} and for in-plane rocking, the Raman peak is noticed at 1174 cm^{-1}. The CH_3 torsion mode for the title molecule is found at 225 cm^{-1} in Raman and calculated at 202 cm^{-1}. All vibrations are well matched with the literature [33].

3.3. NMR spectral calculations

The optimized structure of the molecule is used along with the GIAO method to obtain the chemical shift data of the 4MPPB. The experimental data acquired from DMSO d_6 solvent. The both obtained data are presented in Table 3. The NMR (1H and ^{13}C) computational and experimental spectra are shown in Figures 5 and 6. The C11 available in the carbonyl group having the signal 192.33 ppm in theoretical spectrum and 189.49 ppm in experimental. These data are well matched with literature [34]. The aromatic carbon chemical shift values are usually arising in the region 175-100 ppm [35]. The carbon atoms in the phenyl ring having chemical shift values in the region 144.2 to 112.5 ppm. The C16 atom having highest deshielded signal at 142.11 ppm in experimental and 144.85 ppm in computational section due to the presence of oxygen atom adjacent to it. The C30 atom executed signal at 55.38 ppm in theoretical and 55.55 ppm in experimental part because of the existence of the hydrogen atoms nearer to the C30 atom. Hence in this molecule the C30 and C11 atoms had highest deshielded and shielded signal respectively. The hydrogen atoms present in the title molecule having the chemical shift values in the region of 7.79 to 3.89 ppm in experimental and 8.44 to 3.82 ppm in computational section.

3.4. UV-Vis analysis

The UV-Visible spectral studies performed to determine the charge transfer nature of the title molecule. The experimental studies carried out in DMSO solvent. The previous studies reveal that the TD-DFT is most suitable computational tool to determine the dynamic and static properties of the organic compounds in excited state [36, 37, 38]. The computational absorption maximum, excitation energy, oscillator strength and band gap energy of the 4MMPB are carried out by TD-DFT method in two different correlations functional like CAM-B3LYP and B3LYP with same basis level in IEFPCM model. The computational (CAM-B3LYP) and experimental spectra is presented in Figure 7. The oscillator strengths (f), absorption wavelengths (λ), excitation energies (E) and the major contributions to the electronic transition are mentioned in Table 4.

In the 4MPPB, the experimental absorption peaks observed at 305, 259 nm. The corresponding computational peaks found at 339.71, 319.25, 297.93 nm in CAM-B3LYP method and 399, 376.13, 337.01 nm in B3LYP method. Both the theoretical results are compared and it is found that, the CAM-B3LYP results are well matched with the experimental results. For this reason ultimately experimental and CAM-B3LYP results are compared with each other. The maximum absorption peak in experimental is 305 nm and related theoretical peak found at 297.93 nm. The corresponding oscillator strength is 0.5118 and major contribution of maximum wavelength is H-1- > LUMO (70%), HOMO- > LUMO (13%).

3.5. HOMO-LUMO studies

HOMO and LUMO provide information about the electron affinity and ionization potential of the molecule. The electron accepting ability, electron-donating ability and kinetic stability concerned to the molecule is attained by HOMO-LUMO energy gap [39, 40]. The energy difference between HOMO and LUMO indicating energy gap and it is calculated using the DFT method [41]. The LUMO+3, LUMO+2, LUMO+1, LUMO and HOMO-3, HOMO-2, HOMO-1, HOMO energies and the energy gap for the 4MPPB molecule has been calculated. Figure 8 shows the two dimensional image of the LUMO, LUMO+1, LUMO+2, LUMO+3 and HOMO, HOMO-1, HOMO-2, HOMO-3 orbitals obtained in gas phase using optimized structure of the molecule. The energies of HOMO,

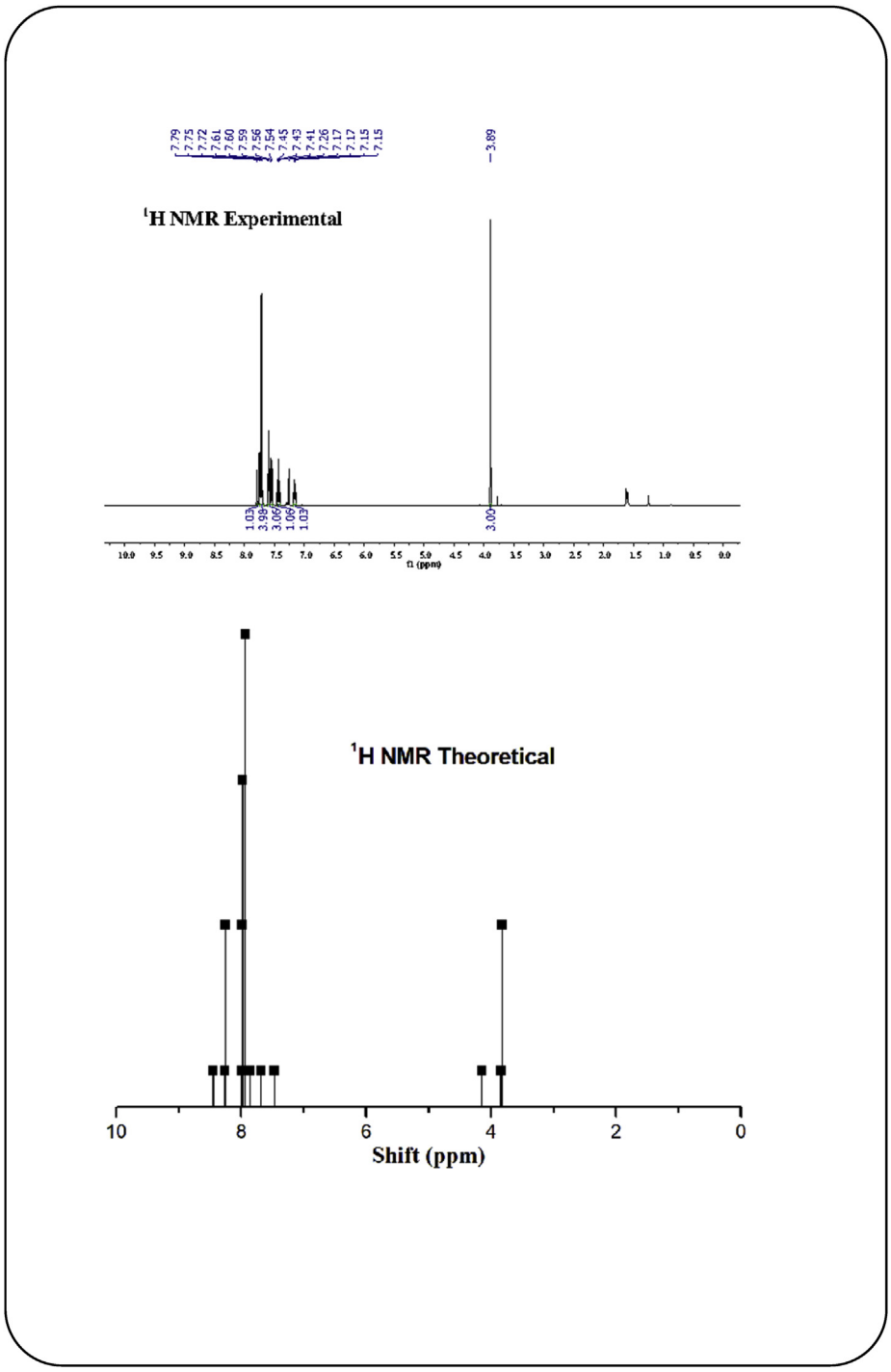

Figure 5. ^{1}H NMR spectrum of 4MPBP (Experimental and Theoretical).

HOMO-1, HOMO-2, HOMO-3 are -6.66, -7.15, -7.37, -7.51 eV respectively and the energies of LUMO, LUMO+1,LUMO+2, LUMO+3 are -3.06, -1.73, -1.37, -0.55 eV respectively. The energy gap between HOMO-LUMO is 3.6 eV. The small energy gap indicates high polarizability and hence this considered chalcone expected promising NLO futures. The ionization potential and chemical hardness of the molecule are calculated by Koopman's theorem [42] presented in Table 5. Large energy gap indicate molecule is hard and soft indicates energy gap is small. The energy gap of the 4MPPB is 3.6 eV. Hence we can say the molecule is soft as well as reactive.

3.6. Molecular electrostatic potential surface (MEP) analysis

The MEP analysis is employed to study the relative reactivity positions for nucleophilic and electrophilic attack [43]. The MEP surface map of the title molecule is obtained by DFT calculation using optimized

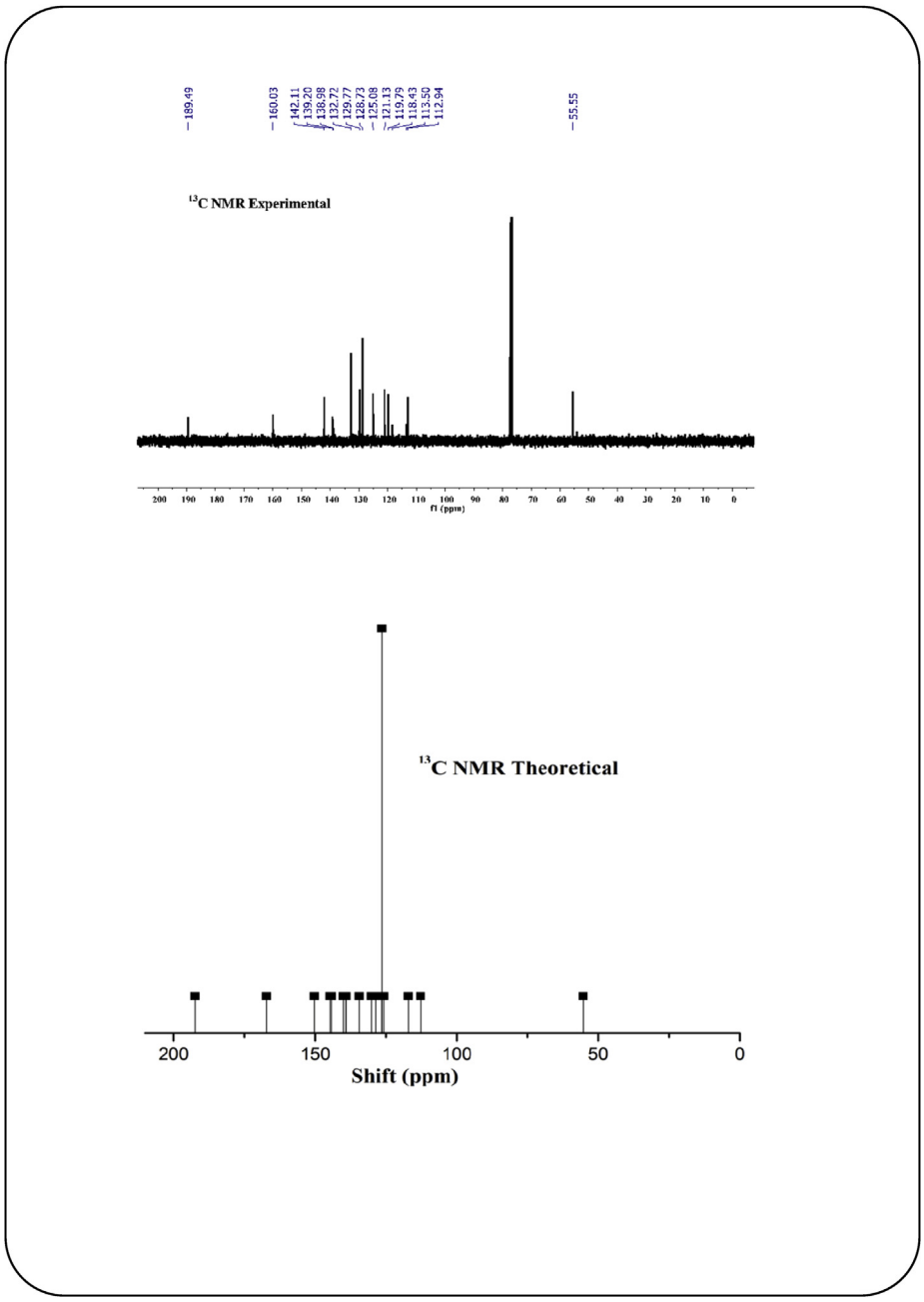

Figure 6. ^{13}C NMR spectrum of 4MPPB (Experimental and Theoretical).

structure and presented in Figure 9. MEP map provides the most vital information regarding the shape, size and charge region existing in the molecule and also offers information regarding the total charge distribution which results in the net electrostatic effect [44]. The obtained MEP map presented with various colors from red to blue. The electrostatic potential is responsible for color coding of the surface (more electron rich region noticed by the red color and more electron poor region noticed by the blue color). Color code indicating increasing order of electrostatic potential is red < orange < yellow < green < blue.

In the title molecule, the electropositive sites moderately spread over the hydrogen atoms. Uppermost electropositive area is located about the H28 hydrogen atom present in the ethylenic bridge because this atom is present with highly electronegative oxygen atom. The nitrogen atom in C≡N having uppermost electronegative and next uppermost electronegative area exists around oxygen atom in carbonyl group. The small amount of electronegative region is situated around the oxygen atom in the methoxy group.

3.7. Natural bond orbital (NBO) analysis

Investigation of NBO is proficient tool to determine inter and intra molecular bonding interactions, and also offers an appropriate foundation for studying the charge transfer in molecular structure [45].

To understand numerous second order interaction amid the unfilled orbital of the one subsystem to the packed orbital of the other subsystem the NBO 3.1 [46] is used with DFT method and it deduce the hyper-conjugation. Hyperconjugative interaction energy of 4MPPB is

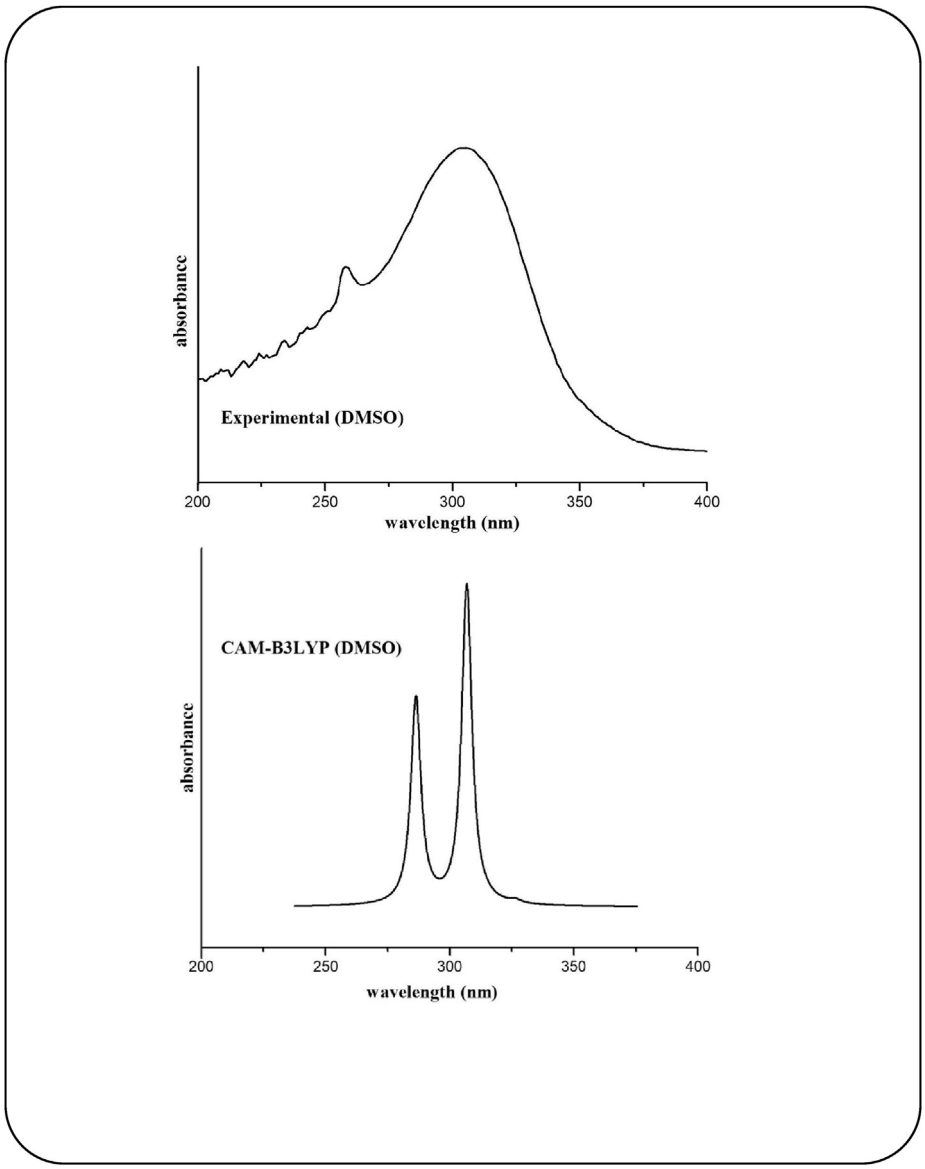

Figure 7. Uv-Vis spectrum of 4MPPB (Experimental and Theoretical).

predicted using the second order perturbation. The hyper-conjugation interaction results in stable outcome of the molecule; this outcome is a result of the overlap of filled orbital by means of the very subsequent electron deficient orbital. This interaction of non-covalent bonding neatly articulated by NBO examination in second order perturbation interaction energy E (2). Larger the value of E (2) represents that electron donor and electron acceptors present in the molecule have high capability of interaction. The available serious interactions are collected in Table 6.

In the present study, the intensive interaction present among π (C2–C3) → π*(C1–C6/C4–C5) (21.18/17.68 kJ/mol) (C4–C5)→π*(C1–C6/C2–C3) (18.73/19.85 kJ/mol). Along with them, certain major lone pair interactions are also listed in Table 6 such as LP (1)C19→ π*(C14–C15/C17–C18) (61.36/59.22 kJ/mol) be there. Among these every interaction the lone pair carbon in phenyl ring attached to C≡N is having the highest E (2) 61.36 kJ/mol.

3.8. NLO studies

Nonlinear optical analysis is prominent notion in the current years because of the impact in area of optoelectronics. According to data of previous studies there are no NLO studies took on the present molecule.

Thus focus is to calculate mean first-order hyperpolarizability (β), the mean polarizability (α) and total static dipole moment (μ) of the molecule

Table 4. The UV–Vis wavelength (λ), band gap energy (E), and oscillator strength (f) for 4MPPB calculated by TD-DFT/B3LYP/6–311++G (d, p) method.

Experimental DMSO		B3LYP/6–311++G (d, p) DMSO				In solvent Major contribution
λ max (nm)	Band gap (ev)	λ cal (nm)	Energy (cm-1)	Band gap (ev)	f (O.S)	
259	4.7906	297.93	33564.76	4.1646	0.5118	H-1- > LUMO (70%), HOMO- > LUMO (13%)
-	-	319.25	31323.35	3.8866	0.762	H-1- > LUMO (20%), HOMO- > LUMO (68%)
305	4.0680	339.71	29436.82	3.6524	0.0079	H-4- > LUMO (75%), H-4- > L+1 (12%)

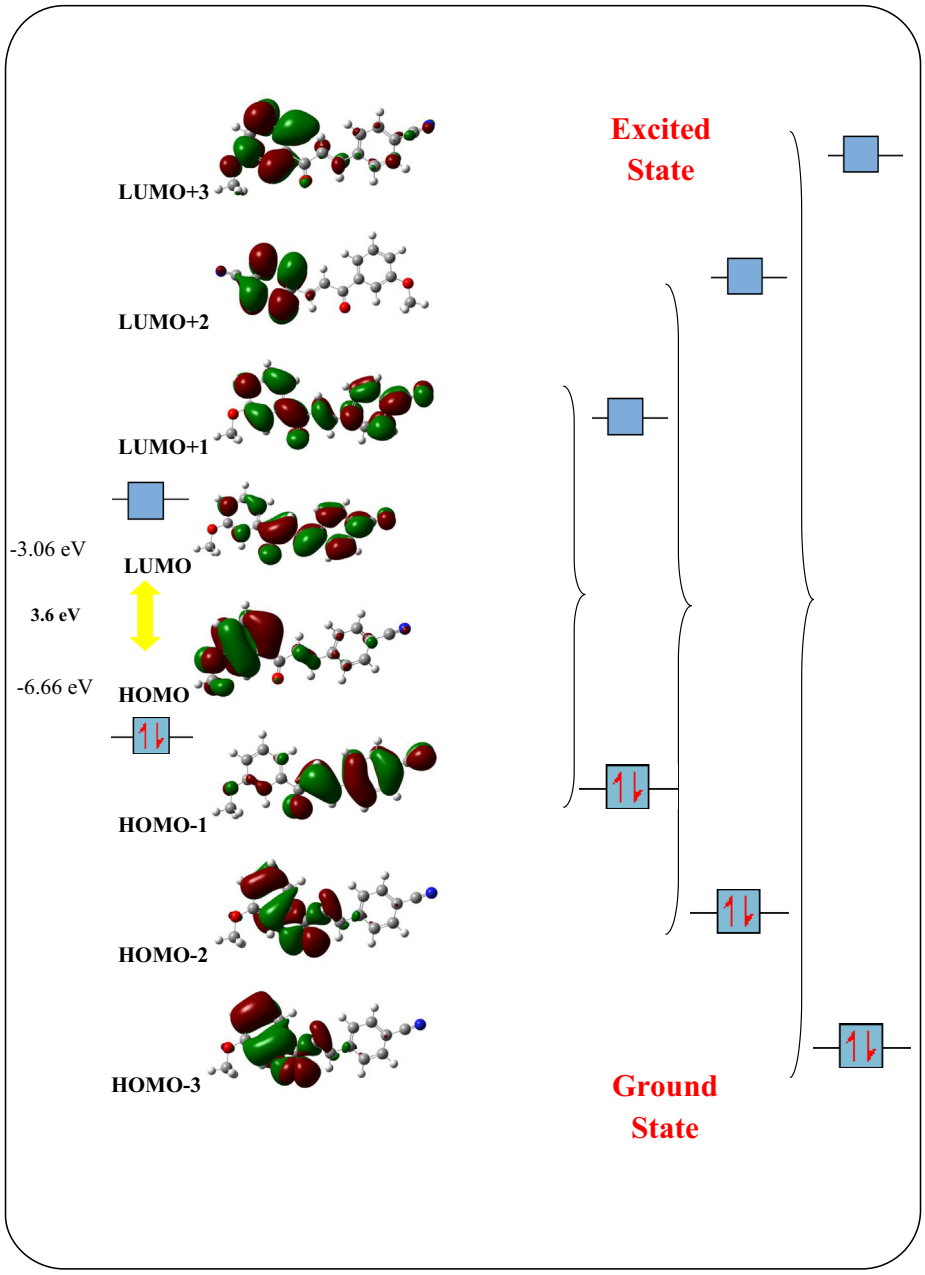

Figure 8. HOMO-LUMO orbitals of 4MPPB.

Table 5. Calculated energy values of 4MPPB molecule by DFT/B3LYP/6–311++G (d, p) method.

Parameters	DFT (eV)
E_{HOMO} (eV)	-6.66
E_{LUMO} (eV)	-3.06
Ionization potential	6.66
Electron affinity	3.06
Energy gap	3.6
Electronegativity	4.86
Chemical potential	-4.86
Chemical hardness	1.8
Chemical softness	0.555 $(eV)^{-1}$
Electrophilicity index	6.561

using DFT method. The results have been presented in Table 7. The consequential values obtained from Gaussian are in form of atomic units (a.u). The acquired data are articulated in terms of standard units by using the relation 1a.u = 2.5412 Debye, 1a.u. = 0.1482×10^{-24} esu and 1 a. u. = 8.6393×10^{-33}esu for μ, α and β respectively [47]. To examine the NLO characteristics of organic compounds urea is taken as standard molecule. Thus for comparative study urea is computed through same basis set. The μ of 4MPPB acquired by DFT method is 4.2369 D and equated through urea (μ = 3.8903D) and the β of 4MPPB is 10.0499×10^{-30} esu and is equated with to urea ($\beta_{tot} = 0.6218 \times 10^{-30}$ esu). Hence Hyperpolarizability of present molecule is found to be 16 times greater than the reference material urea. Ram Kumar *et al.* [25] reported the comparable type of the molecule possessing β_{tot} is 10.116×10^{-30} esu and μ = 1.7188 D. Pramod *et al.* [48] studied the NLO characteristics of the same derivatives; the β_{tot} is 16.45×10^{-30} esu and μ = 4.72 D. The

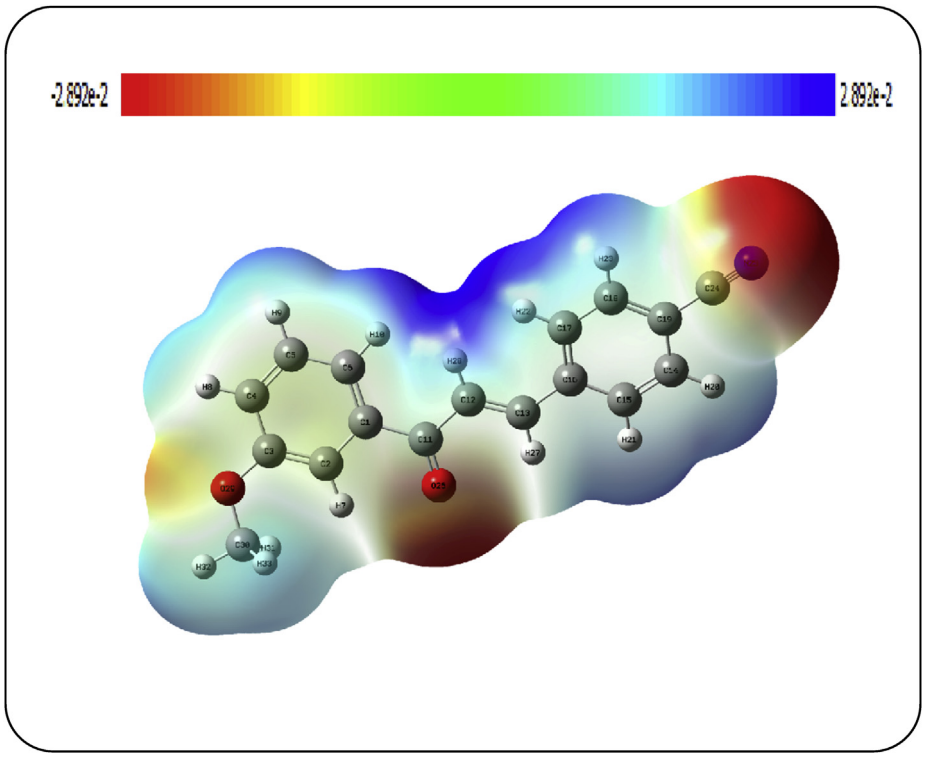

Figure 9. MEP surface of 4MPPB.

Table 6. Selected second order perturbation theory analysis of Fock matrix in NBO basis of 4MPPB.

Donor (i)	Type of Band	Occupancy	Acceptor (j)	Type of Band	Occupancy	E2 (Kj/mol)a	E(j)-E(i) (a.u)b	F (i, j) (a.u)c
C1–C6	π	1.65969	C2–C3	π*	0.34754	17.46	0.28	0.063
	π	1.65969	C4–C5	π*	0.30453	19.74	0.28	0.068
	π	1.65969	C11–O26	π*	0.2008	18.12	0.27	0.065
C2–C3	π	1.65152	C1–C6	π*	0.37644	21.18	0.29	0.071
	π	1.65152	C4–C5	π*	0.30453	17.68	0.29	0.065
C4–C5	π	1.68975	C1–C6	π*	0.37644	18.73	0.29	0.066
	π	1.68975	C2–C3	π*	0.34754	19.85	0.29	0.068
C12–C13	π	1.8369	C11–O26	π*	0.2008	19.36	0.3	0.069
C19	LP1	1.06089	C14–C15	π*	0.28922	61.34	0.15	0.105
	LP1	1.06089	C17–C18	π*	0.27202	59.22	0.15	0.104
N25	LP1	1.97165	C19–C24	σ*	0.03149	11.47	1.01	0.096
O26	LP2	1.88756	C1–C11	σ*	0.06416	18.47	0.69	0.102
	LP2	1.88756	C11–C12	σ*	0.05901	19.19	0.69	0.104
O29	LP2	1.83972	C2–C3	π*	0.34754	30.15	0.34	0.095

4MPPB values are comparable with the reported data. Therefore, it can be stated that 4MPPB can be utilized to investigate the profoundly nonlinear optical properties.

3.9. ELF and LOL analysis

Electron localization function (ELF) and localized orbital locator (LOL) are carried out by Multiwfn software. ELF and LOL tools are useful to recognize the places of bond pairs, lone pairs and size of the bonding the title molecule [49]. Color map of ELF and LOL gives information concerned to the electron density charge distribution. Figure 10 (a) and 10 (b) represents the two dimensional color shade maps of the ELF and LOL. The ELF map lies in the range 0.0–1.0. In the ELF map the white color indicates upper limit of the ELF scale (1.0) whereas middle ELF scale (0.5) is represented by yellow to green and blue color indicates the lower limit of the ELF scale. In the color map, completely delocalised electron regions are indicated by smaller value of (<0.5) of ELF but the greater value s of the ELF (ELF $= 1.0$) indicates nonbonding and bonding localized electron areas. ELF and LOL values are in the similar range. In Figure 10(a), the high ELF regions are observed about the hydrogen atom which indicates the high localization of boding and non-bonding electrons. The presence of delocalisation cloud is indicated by blue region present around oxygen and carbon atoms. In Figure 10(b), covalent regions are observed between carbon and carbon atoms of the benzene ring which is represented by red color with high LOL value.

3.10. Fukui function analysis

Fukui function is employed to explore the local reactivity parameters of the molecule. These functions are obtained via clear difference when an electron is removed or added from molecule. The dissimilarity in charge density among charged and neutral molecules gives the Fukui

Table 7. NLO properties of 4MPPB molecule.

Parameter	a.u	esu (x10^{-24})	Parameter	a.u	esu (x10^{-33})
α_{xx}	425.95324	63.12627	β_{xxx}	-427.37843	-3.6922505
α_{xy}	-2.45765	-0.364225	β_{yxx}	-831.82927	-7.1864226
α_{yy}	207.99505	30.82486	β_{xyy}	-329.91218	-2.8502103
α_{xz}	-0.65440	-0.09698	β_{yyy}	-66.04429	-0.5705758
α_{yz}	-2.44199	-0.36190	β_{zxx}	79.55212	0.6872746
α_{zz}	111.56284	16.53361	β_{xyz}	-12.71282	-0.1098299
α_0	248.50371	36.82825	β_{zyy}	2.11686	0.0182882
$\Delta\alpha$	278.96719	41.34293	β_{xzz}	5.39462	0.0466057
μ_x	1.65908	4.21607	β_{yzz}	14.34947	0.1239694
μ_y	0.16228	0.41241	β_{zzz}	3.54630	0.0306376
μz	-0.03233	-0.08217	β_0	1163.2815	10.049938
μ	1.66732	4.23699	-	-	-

function. In the singlet state the neutral 4MPPB posse's lowest energy. In the doublet state the charge densities of cation and anion of 4MPPB can be evaluated [50].

Fukui function is calculated by

$$f_k^+ = q_k(N+1) - q_k(N) \quad (1)$$

$$f_k^- = q_k(N-1) - q_k(N) \quad (2)$$

$$\Delta f(r) = f_k^+ - f_k^- \quad (3)$$

The dual descriptor Δf envisage the reactive sites of the title molecule in an efficient manner. The spot is suitable for a nucleophilic attack if $\Delta f(r) > 0$ whereas spot is suitable for an electrophilic attack is given by $\Delta f(r) < 0$. The Fukui functions ($f_k^+ .f_k^- .f_k^0$) and dual descriptor (Δf) of the present molecule is calculated and mentioned in Table 8. The atoms with $\Delta f_k > 0$ data are expected in the order of O29 > H33 = H10 > H31 > H20 = H21 > C6 > H32 and these sites are appropriate for nucleophilic attack. The atoms having values of $\Delta f_k < 0$ values are expected in the order of O26 > H28 > C30 > C13 > C11 and are possible spots for nucleophilic attack.

3.11. Drug-likeness

The important ADME variables like Hydrogen bond donors (HBD), hydrogen bond acceptors (HBA), Blood-brain barrier penetration (BBB), molar refractivity (MR), logkp, Topological polar surface area (TPSA) and bioavailability score of 4MPPB are computed and shown in Table 9. From the literature it is analyzed that values of HBA and HBD values should be less than 10 and 5 respectively. For the title molecule HBA and HBD values are calculated as 3 and 0. The highest value of TPSA is 140 Å^2 and in the present work it is calculated as 50.09 Å^2. The value of molar refractivity lies in the range of 40 and 130. The MR value of the title molecule is 77.46. Table 9 reflects that high GI absorption side, skin permeability (log Kp) observed as-5.51and bioavailability value of 0.55. The above said results depicts that the 4MPPB has agreeable biological properties.

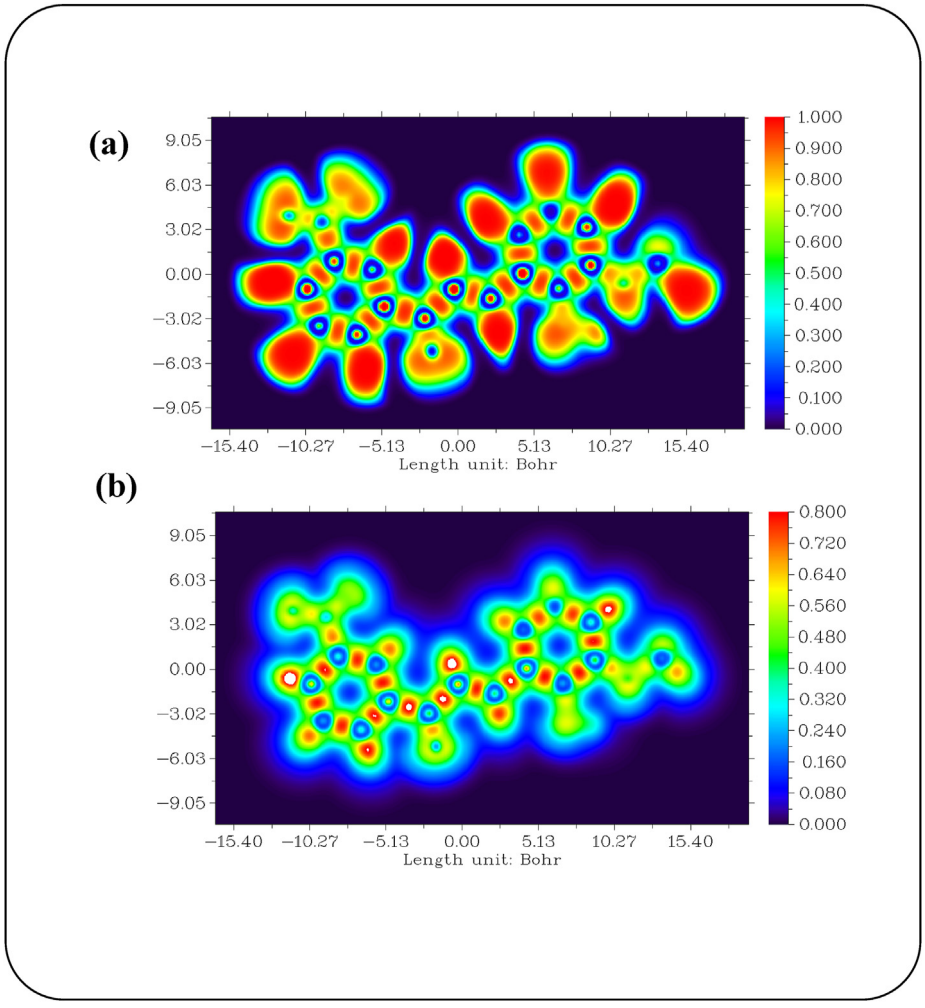

Figure 10. (a) ELF color map and (b) LOL color map 4MPPB molecule.

Table 8. Local reactivity descriptors of 4MPPB molecule.

Atom	Mulliken Atomic Charge			Fukui Functions			$\Delta f = f_k^+ - f_k^-$
	Neutral q(N)	Cation q (N-1)	Anion q (N+1)	Nucleophilic attack (f_k^+)	Electrophilic attack (f_k^-)	Radical attack (f_k^0)	
C1	0.027	0.030	0.028	0.002	-0.001	0.001	0.003
C2	-0.152	-0.180	-0.110	-0.028	-0.041	-0.035	0.013
C3	0.270	0.261	0.279	-0.009	-0.009	-0.009	0.000
C4	-0.101	-0.126	-0.064	-0.025	-0.037	-0.031	0.012
C5	-0.145	-0.150	-0.136	-0.005	-0.009	-0.007	0.004
C6	-0.127	-0.138	-0.086	-0.011	-0.041	-0.026	0.030
H7	0.171	0.144	0.216	-0.027	-0.044	-0.036	0.018
H8	0.147	0.097	0.210	-0.050	-0.063	-0.057	0.013
H9	0.133	0.090	0.192	-0.042	-0.059	-0.051	0.017
H10	0.130	0.112	0.182	-0.017	-0.053	-0.035	0.035
C11	0.225	0.186	0.241	-0.039	-0.017	-0.028	-0.023
C12	-0.119	-0.152	-0.100	-0.033	-0.019	-0.026	-0.014
C13	-0.139	-0.186	-0.119	-0.047	-0.021	-0.034	-0.026
C14	-0.093	-0.112	-0.079	-0.019	-0.014	-0.016	-0.005
C15	-0.180	-0.198	-0.161	-0.018	-0.019	-0.019	0.001
C16	0.109	0.113	0.108	0.005	0.000	0.002	0.004
C17	-0.146	-0.171	-0.130	-0.025	-0.016	-0.020	-0.010
C18	-0.095	-0.109	-0.081	-0.014	-0.014	-0.014	-0.001
C19	0.104	0.071	0.125	-0.033	-0.021	-0.027	-0.012
H20	0.164	0.109	0.204	-0.055	-0.039	-0.047	-0.016
H21	0.152	0.104	0.187	-0.048	-0.035	-0.041	-0.014
H22	0.142	0.104	0.163	-0.039	-0.021	-0.030	-0.018
H23	0.162	0.110	0.198	-0.052	-0.036	-0.044	-0.016
C24	-0.066	-0.117	-0.030	-0.051	-0.036	-0.044	-0.015
N25	-0.212	-0.286	-0.156	-0.073	-0.057	-0.065	-0.016
O26	-0.423	-0.512	-0.385	-0.089	-0.038	-0.063	-0.051
H27	0.170	0.115	0.207	-0.055	-0.037	-0.046	-0.018
H28	0.140	0.087	0.164	-0.053	-0.024	-0.039	-0.029
O29	-0.551	-0.569	-0.466	-0.018	-0.086	-0.052	0.068
C30	-0.174	-0.158	-0.218	0.016	0.044	0.030	-0.028
H31	0.156	0.147	0.199	-0.009	-0.043	-0.026	0.034
H32	0.170	0.139	0.222	-0.031	-0.052	-0.041	0.021
H33	0.154	0.145	0.197	-0.008	-0.043	-0.026	0.035

Table 9. ADME properties of 4MPPB.

Compound	HBD	HBA	MR	TPSA Å^2	GI absorption	BBB permanent	CYP1A2 inhibitor	Log Kp (cm/s)	Lipinski violations	bioavailability
4MPPB	0	3	77.46	50.09	High	Yes	Yes	-5.51	0	0.55

D - Hydrogen Bond Donor, HBA - Hydrogen bond acceptor, MR - Molar refractivity, TPSA - Topological polar surface area, GI - Gastrointestinal, BBB - blood–brain barrier penetration, log kp – skin permeability.

3.12. Molecular docking studies

Severe acute respiratory syndrome corona virus (SARS-CoV) is global problem across world. Corona viruses belong to the family of Corona viridae, which is a group of enveloped single stranded-positive sense RNA virus SARS-CoV spreads commonly from person to person and is quickly evolving the globes most important source of bereavement. Preclinical symptoms of this disease include high fever, headache, dry cough, and shortness of breath. Severe infection leads to pneumonia and kidney failure [51, 52, 53]. Currently, no effective antiviral medication are existing for SARS-CoV-2, and they need to be developed immediately. Viral proteases have been recognized as the reliable targets for the SARS-CoV-2. Inhibitors of viral proteases are largely valuable drugs and are extensively used in field of clinical practice. Generally, these viruses harvest quite a few polypeptides that encourage proteolytic collapse to generate 20 extra proteins in the time of their lifecycle.

Among them two proteases are vital for virus replication which includes chief protease (M^{PRO}) defined as 3 C-like protease ($3CL^{PRO}$) and papain-like protease (PL^{PRO}) [54, 55, 56]. M^{PRO} and PL^{PRO} process the polypeptide pp1a and pp1ab in a sequence specific manner to generate 16 dissimilar non-structural proteins. M^{PRO} is long 306 amino acid and it comprises of three domains *N*-terminal domain-I, *N*-terminal domain-II, and C-terminal domain-III. On the other hand, PL^{PRO} is an essential component of the replicase-transcriptase complex. The PL^{PRO} processes the poly protein which generates non-structural proteins 1–4. The two proteases M^{PRO} and PL^{PRO} are evenly vital for viral lifecycle and their genome encrypts two poly proteins, pp1a and pp1ab for the period of their conversion phase throughout ribosomal frame shifting method [57]. The development of small molecule inhibitors against M^{PRO} and PL^{PRO} is considered to have possible therapeutic objective for the dealing of SARS-CoV-2. At the phase of drug design for SARS-CoV-2, primary troubles know the interface among the drugs and their receptors.

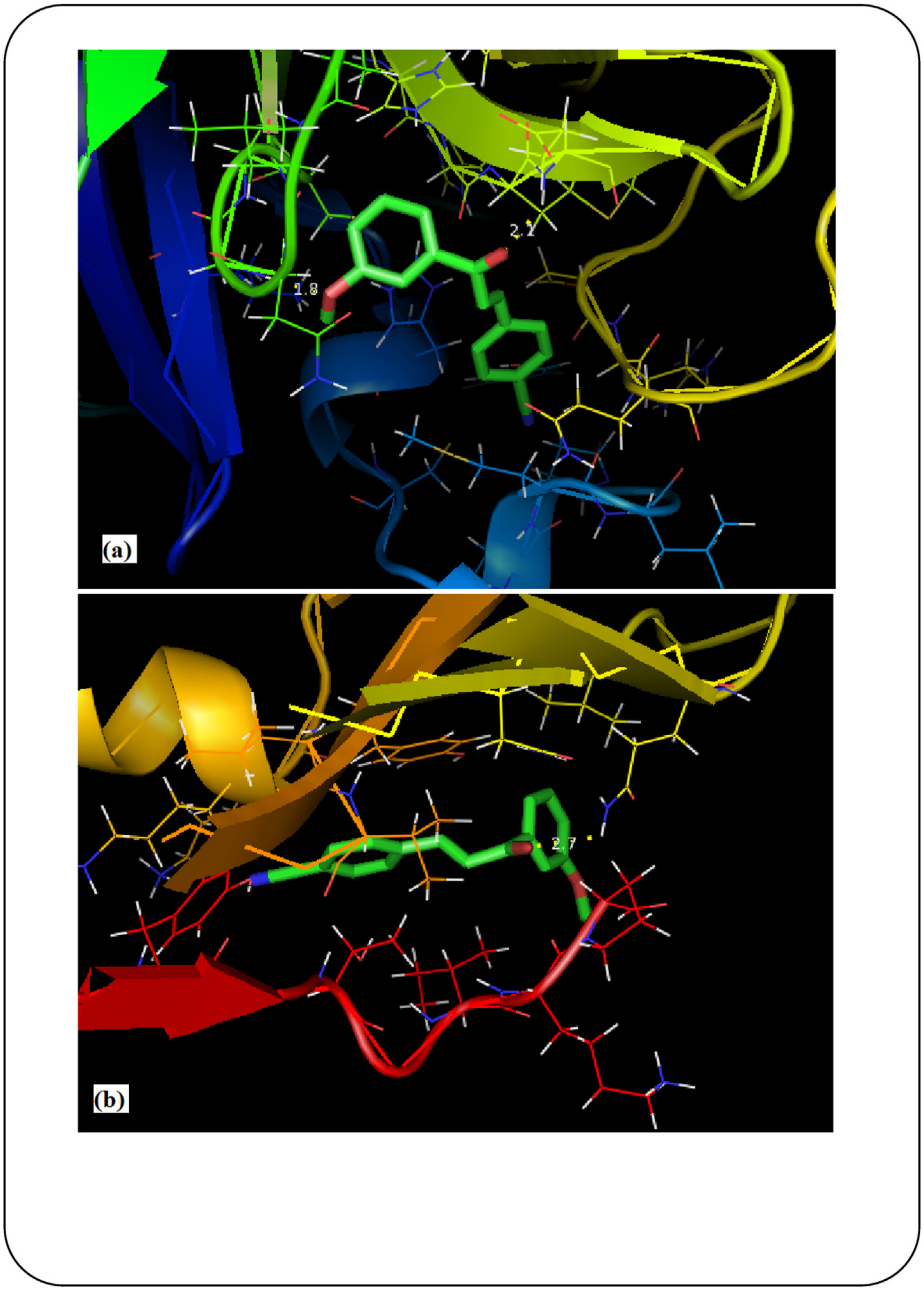

Figure 11. Lowest energy docked poses of the 4MPPB with various protein target of (a) M^{PRO} and (b) PL^{PRO}.

Table 10. The obtained docking parameters of the 4MPPB and their rank calculated by Autodock.

Ligand	Target protein (receptor)	Protein (PDB ID)	Docking Parameters based on the rank								
			Binding energy (Kcal/mol)			Estimated Inhibition constant (micromolar - μm)			Intermolecular energy (Kcal/mol)		
			1	2	3	1	2	3	1	2	3
4MPPB	M^{PRO}	6LU7	-7.76	-7.19	-7.12	2.05	5.40	6.04	-8.95	-8.38	-8.31
	PL^{PRO}	6WUU	-6.50	-6.27	-5.86	17.27	25.43	50.83	-7.69	-7.46	-7.05

Molecular docking is one of the techniques used to investigate the interaction of drug receptor complex.

Molecular docking is important method employed for designing of drug that is effectively utilized to envisage the chosen binding orientation of tiny compounds on the protein surface to create a constant complex. Crystal structure of M^{PRO} (PDB ID: 6LU7) and PL^{PRO} (PDB ID: 6WUU) receptors are recorded by PDB. Docking computations are performed by Auto Dock 4.2 program. The ensuing docking validations are consequently grouped with a RMSD and are graded with the help of binding energy values. PyMol [58] software is used to visualise the docked results. In the current investigation, the potency of inhibition of 4MPPB against M^{PRO} and PL^{PRO} receptors has been performed using molecular docking studies. Figure 11 depicts the formation of hydrogen bonds via length of the hydrogen bonds by means of amino acid protein

molecule. The hydrogen bond creation among target protein and ligand is indicated by dotted yellow lines. By performing docking studies, we can obtain the values of binding interactions, together with inhibition constant, binding energy, and intermolecular energy among M^{PRO} and PL^{PRO} receptors and 4MPPB ligand in the most excellent results are collected in Table 10. The performed docking studies reveal that 4MPPB ligand exhibits excellent inhibiting characteristic for the cure of SARS-CoV-2.

4. Conclusion

The successful synthesizes of the title molecule is followed by its characterization using various spectroscopic techniques. The computational and experimental geometrical parameters are in good agreement. FT-Raman and FT-IR spectral values procured by experimental study are comparable to computed spectral data acquired by DFT technique. In NMR studies, we observed that major shielded signal is present around C16 atom. The experimental absorption wavelength and theoretical values obtained by CAM-B3LYP method are in good agreement. The FMO study revealed that the energy gap of 4MPPB is 3.6 eV, it reveals that the molecule is soft in nature and exhibit reactive property. From MEP surface analysis it can be concluded that, the highest electronegative area is located about the nitrogen atom present in C≡N. From NBO study, we found that LP (1) C19→ π*(C14–C15) (61.36 kJ/mol) is having highest stabilization energy because the C19 atom in phenyl ring2 attached to C≡N. The NLO study shows that the title molecule is good for further nonlinear analysis. The major ELF areas are found about hydrogen atom showed the major localization of non-bonding and boding electrons. In Fukui function, the atoms with values of $\Delta f_k < 0$ values are estimated in the order of O26 > H28 > C30 > C13 > C11 and are the spots suitable for nucleophilic attack. The drug-likeness parameters reflect that 4MPPB has adequate biological properties.

Declarations

Author contribution statement

Shivaraj B. Radder: Performed the experiments; Wrote the paper.

Raveendra Melavanki; Seema S. Khemalapure: Conceived and designed the experiments; Contributed reagents, materials, analysis tools or data.

Sudhir M. Hiremath: Conceived and designed the experiments; Analyzed and interpreted the data; Wrote the paper.

Raviraj. Kusanur: Contributed reagents, materials, analysis tools or data.

S. Christopher Jeyaseelan: Analyzed and interpreted the data.

Funding statement

This research did not receive any specific grant from funding agencies in the public, commercial, or not-for-profit sectors.

Data availability statement

Data included in article/supplementary material/referenced in article.

Declaration of interests statement

The authors declare no conflict of interest.

Additional information

No additional information is available for this paper.

References

[1] M. Anis, G.G. Muley, A. Hakeemd, M.D. Shirsat, S.S. Hussaini, Exploring the influence of carboxylic acids on nonlinear optical (NLO) and dielectric properties of KDP crystal for applications of NLO facilitated photonic devices, Opt. Mater. 46 (2015) 517–521.

[2] L. Kamath, K.B. Manjunatha, S. Shettigar, G. Umesh, B. Narayana, S. Samshuddin, B.K. Sarojini, Investigation of third-order nonlinear and optical power limiting properties of terphenyl derivatives, Opt Laser. Technol. 56 (2014) 425–429.

[3] M. Anis, S.S. Hussaini, A. Hakeem, M.D. Shirsat, G.G. Muley, Synthesis, growth and optical studies of novel organometallic NLO crystal: calcium bis-thiourea chloride, Optik 127 (2016) 2137–2142.

[4] M. Shkir, S. Muhammad, S. AlFaify, A. Irfan, P.S. Patil, M. Arora, H. Algarnia, Z. Jingping, Investigation on the key features of D-π-A type novel chalcone derivative for optoelectronic applications, RSC Adv. 5 (2015) 87320–87332.

[5] A. Kumar, R. Kumar, A. Gupta, P. Tandon, E. Deepak D'silva, Molecular structure, nonlinear optical studies and spectroscopic analysis of chalconederivative (2E)-3-[4-(methylsulfanyl) phenyl]-1-(3-bromophenyl) prop-2-en-1-one by DFT calculations, J. Mol. Struct. 1150 (2017) 166–178.

[6] J. Indira, P. Prakash Karat, B.K. Sarojini, 3-[4-(Dimethylamino)phenyl]-1-(2-pyrrolyl)prop-2-en-1-one, J. Cryst. Growth 242 (2002) 209–214.

[7] S. Alen, D. Sajan, K. Chaitanya, V. Shettigar, V. BenaJothy, Synthesis, growth, vibrational spectral investigations and structure-property relationship of an organic NLO crystal: 3, 4 dimethoxy chalcone, Chem. Phys. Lett. 636 (2015) 208–215.

[8] M. Aneta, P. Catherine, A. Geetha, Nancy E. Davidson, H. Peng, Saeed R. Khan, Anticancer activities of novel chalcone and bis-chalcone derivatives, Bioorg. Med. Chem. 14 (2006) 3491–3495.

[9] S.F. Nielsen, T. Boesen, M. Larsen, H. Kromann, Antibacterial chalcones—bioisosteric replacement of the 4'-hydroxy group, Bioorg. Med. Chem. Lett 12 (2004) 3047–3054.

[10] A.K. Padersen, G.A. Fitz, Preparation and analysis of deuterium-labeled aspirin: application to pharmacokinetic studies, J. Pharmacol. Sci. 74 (1985) 188–192.

[11] A. Valla, B. Valla, D. Cartier, Schrevel, New syntheses and potential antimalarial activities of new 'retinoid-like chalcones, Eur. J. Med. Chem. 41 (2005) 142–146.

[12] Y. Satomi, Inhibitory effects of 3′-methyl-3-hydroxy-chalcone on proliferation of human malignant tumor cells and on skin carcinogenesis, Indian J. Cancer 55 (1993) 506–514.

[13] R. Kusanur, M. Ghate, M.V. Kulkarni, Synthesis of spiro[indolo-1,5-benzodiazepines] from 3-acetyl coumarins for use as possible antianxiety agents, J. Chem. Sci. 116 (2004) 265–270.

[14] D. Patagar, R. Kusanur, N.D. Sitwala, M.D. Ghate, S. Saravanakumar, S. Nembenna, P.A. Gediya, Synthesis of novel 4-substituted coumarins, docking studies, and DHODH inhibitory activity, J. Het. Chem. 56 (2019) 2761–2771.

[15] M.J. Frisch, G.W. Trucks, H.B. Schlegel, G.E. Scuseria, M.A. Robb, J.R. Cheeseman, J.A. Montgomery Jr., T. Vreven, K.N. Kudin, J.C. Burant, J.M. Millam, S.S. Iyengar, J. Tomasi, V. Barone, B. Mennucci, M. Cossi, G. Scalmani, N. Rega, G.A. Petersson, H. Nakatsuji, M. Hada, M. Ehara, K. Toyota, R. Fukuda, J. Hasegawa, M. Ishida, T. Nakajima, Y. Honda, O. Kitao, H. Nakai, M. Klene, X. Li, J.E. Knox, H.P. Hratchian, J.B. Cross, C. Adamo, J. Jaramillo, R. Gomperts, R.E. Stratmann, O. Yazyev, A.J. Austin, R. Cammi, C. Pomelli, J.W. Ochterski, P.Y. Ayala, K. Morokuma, A. Voth, P. Salvador, J.J. Dannenberg, V.G. Zakrzewski, S. Dapprich, J.A. Pople, Gaussian Inc., Wallingford, CT, 2004.

[16] A.B. Nielsen, A.J. Holder, Gauss View 5.0 User's Reference, Gaussian Inc, Pittsburgh.

[17] S.M. Hiremath, A. Suvitha, N.R. Patil, C.S. Hiremath, S.S. Khemalapure, S.K. Pattanayak, V.S. Negalurmath, K. Obelannavar, S.J. Armaković, S. Armaković, Synthesis of 5-(5-methyl-benzofuran-3-ylmethyl)-3H-[1, 3, 4] oxadiazole-2-thione and investigation of its spectroscopic, reactivity, optoelectronic and drug likeness properties by combined computational and experimental approach, Spectrochim. Acta, Part A 205 (2018) 95–110.

[18] M.H. Jamroz, Vibrational Energy Distribution Analysis VEDA 4, Warsaw, 2004.

[19] E. Runge, E.K.U. Gross, Density-functional theory for time-dependent systems, Phys. Rev. Lett. 52 (1984) 997–1000.

[20] T. Lu, F. Chem, Multiwfn, A multifunctional wavefunction analyser, J. Comput. Chem. 33 (2012) 580–592.

[21] H.A. Khamees, M. Jyothi, S.A. Khanum, M. Madegowda, Synthesis, crystal structure, spectroscopic characterization, docking simulation and density functional studies of 1-(3,4-dimethoxyphenyl) -3-(4-flurophenyl)-propan-1-one, J. Mol. Struct. 1161 (2018) 199–217.

[22] S.S. Khemalapure, V.S. Katti, C.S. Hiremath, S.M. Hiremath, M. Basanagouda, S B, Radder Spectroscopic (FT-IR, FT-Raman, NMR and UV-Vis), ELF, LOL, NBO, and Fukui function investigations on (5-bromo-benzofuran-3-yl)-acetic acid hydrazide (5BBAH): experimental and theoretical approach, J. Mol. Struct. 1196 (2019) 280–290.

[23] D.N. Sathyanarayana, Vibrational Spectroscopy, Theory and Applications, New Age International Publishers, New Delhi, 2004.

[24] B. Smith, Infrared Spectral Interpretation. A Systematic Approach, CRC Press, Washington, DC, 1999.

[25] Ram Kumar, T. Karthick, P. Tandon, P. Agarwal, A.P. Menezes, A. Jayarama, Structural and vibrational characteristics of a non-linear optical material 3-(4-nitrophenyl)-1-(pyridine-3-yl) prop-2-en-1-one probed by quantum chemical computation and spectroscopic techniques, J. Mol. Struct. 1164 (2018) 180–190.

[26] A.T. Alphonsa, C. Loganathan, S.A.A. Anand, S. Kabilan, Synthesis, spectroscopic investigations (FT-IR, NMR, UV-Vis, and TD-DFT), and molecular docking of (E)-1-(benzo[d][1, 3]dioxol-6-yl)- 3-(6-methoxynaphthalen-2-yl)prop-2-en-1-one, J. Mol. Struct. 1130 (2017) 1018–1023.

[27] S.S. Khemalapure, V.S. Katti, C.S. Hiremath, M. Basanagouda, S.M. Hiremath, S.J. Armaković, S. Armaković, Molecular structure, optoelectronic properties, spectroscopic (FT-IR, FT-Raman and UV–Vis), H-BDE, NBO and drug likeness investigations on 7, 8-benzocoumarin-4-acetic acid (7BAA), J. Mol. Struct. 1195 (2019) 815–826.
[28] G. Socrates, Infrared and Raman Characteristic Group Frequencies, 1 Table and Charts, third ed., Wiley, Chichester, 2001.
[29] G. Varsanyi, Assignments for Vibrational Spectra of 700 Benzene Derivatives, Adam Hilger, London, 1974.
[30] Q. Wu, Y. Chen, D. Chen, Z. Zhou, Synthesis, crystal structure and vibrational properties studies of 2-((4-(4,4,5,5-tetramethyl-1,3,2-dioxaborolan-2-yl)phenoxy) methyl) benzonitrile and N-(3-bromobenzyl)-4-(4,4,5,5-tetramethyl-1,3,2-dioxaborolan-2-yl)aniline, J. Mol. Struct. 1229 (2021) 129782.
[31] N.B. Colthup, L.H. Daly, S.E. Wiberly, Introduction to IR and Raman Spectroscopy, Academic Press, New York, 1990.
[32] K. Thirunavukkarasu, P. Rajkumar, S. Selvaraj, R. Suganya, M. Kesavan, S. Gunasekaran, S. Kumaresan, Vibrational (FT-IR and FT-Raman), electronic (UVeVis), NMR (^{1}H and ^{13}C) spectra and molecular docking analyses of anticancer molecule 4-hydroxy-3-methoxycinnamaldehyde, J. Mol. Struct. 1173 (2018) 307–320.
[33] S. Kaya, H. Gökce, T. Arslan, G. Alpaslan, Synthesis, spectroscopic characterization, DFT computations, nonlinear optical profile and molecular docking study of a novel chalcone derivative, J. Mol. Struct. 1202 (2020) 127270.
[34] M.H. Rahuman, S. Muthu, B.R. Raajaraman, M. Raja, H. Umamahesvari, Investigations on 2-(4-Cyanophenylamino) acetic acid by FT-IR, FT-Raman, NMR and UV-Vis spectroscopy, DFT (NBO, HOMO-LUMO, MEP and Fukui function) and molecular docking studies, Heliyon 6 (2020), e04976.
[35] S.M. Hiremath, S.S. Khemalapure, C.S. Hiremath, A.S. Patil, M. Basanagouda, Quantum chemical computational and spectroscopic (IR, Raman, NMR, and UV) studies on the 5-(5-methoxy-benzofuran-3-ylmethyl)-3H-[1,3,4] oxadiazole-2-thione, J. Mol. Struct. 1210 (2020) 128041.
[36] N. Suma, D. Aruldhas, I. Hubert Joe, A. Ronaldo Anuf, B.S. Arun Sasi, Spectroscopic, quantum chemical, QTAIM analysis, molecular dynamics simulation, docking studies and solvent effect of pyridin-2-yl oxyacetic acid herbicide and its derivatives, J. Mol. Struct. 1206 (2020) 127677.
[37] P.G. Patil, R. Melavanki, S.B. Radder, R. Kusanur, C.S. Hiremath, N.R. Patil, S.M. Hiremath, Synthesis, structural characterizations, and quantum chemical investigations on 1-(3-methoxy-phenyl)-3-naphthalen-1-yl-propenone, ACS Omega 6 (40) (2021) 25982–25995.
[38] M. Raja, R. Raj Muhamed, S. Muthu, M. Suresh, Synthesis, spectroscopic (FT-IR, FT-Raman, NMR, UV–Visible), NLO, NBO,HOMO-LUMO, Fukui function and molecular docking study of (E)-1-(5-bromo-2-hydroxybenzylidene)semicarbazide, J. Mol. Struct. 1141 (2017) 284–298.
[39] Jun-ichi Aihara, Weighted HOMO-LUMO energy separation as an index of kinetic stability for fullerenes, Theor. Chem. Acc. 102 (1999) 134–138.
[40] S.M. Hiremath, A.S. Patil, C.S. Hiremath, M. Basanagouda, S.S. Khemalapure, N.R. Patil, S.B. Radder, S.J. Armaković, S. Armaković, Structural, spectroscopic characterization of 2-(5-methyl-1-benzofuran-3-yl) acetic acid in monomer, dimer and identification of specific reactive, drug likeness properties: experimental and computational study, J. Mol. Struct. 1178 (2019) 1–17.
[41] S.M. Hiremath, Vibrational, electronic and reactivity insight on (5-chloro-benzofuran-3-yl)-acetic acid hydrazide: a Spectroscopic and DFT approach, J. Mol. Struct. 1239 (2021) 130479.
[42] T. Koopmans, Über die Zuordnung von Wellenfunktionen und Eigenwertenzu den Einzelnen Elektronen Eines Atoms, Physica 1 (1934) 104–113.
[43] J.S. Murray, K. Sen, Molecular Electrostatic Potentials Concepts and Applications, Elsevier Science B.V, Amsterdam, The Netherlands, 1996.
[44] S.S. Khemalapure, S.M. Hiremath, C.S. Hiremath, V.S. Katti, M.M. Basanagouda, Investigations of structural, vibrational and electronic properties on 5-(6-methyl-benzofuran-3-ylmethyl)-3H- [1,3,4]oxadiazole-2-thione: experimental and computational approach, Chem. Data Collect. 28 (2020) 100410.
[45] S.S. Khemalapure, S.M. Hiremath, C.S. Hiremath, V.S. Katti, M.M. Basanagouda, G.P. Khanal, T. Karthick, Structural, spectroscopic and computational investigations on (4,6-dimethyl-benzofuran-3-yl)-acetic acid hydrazide, J. Mol. Struct. 1220 (2020) 128748.
[46] E.D. Glendening, A.E. Reed, J.E. Carpenter, F. Weinhold, NBO Version 3.1 Program Manual, TCI, University of Wisconsin, Madison, 1998.
[47] S.M. Hiremath, A. Suvitha, N.R. Patil, C.S. Hiremath, S.S. Khemalapure, S.K. Pattanayak, V.S. Negalurmath, K. Obelannavar, Molecular structure, vibrational spectra, NMR, UV, NBO, NLO, HOMO-LUMO and molecular docking of2-(4, 6-Dimethyl-1-benzofuran-3-yl) acetic acid (2DBAA): experimental and theoretical approach, J. Mol. Struct. 1171 (2018) 362–374.
[48] B. Pramodh, N.K. Lokanath, S. Naveen, P. Naresh, S. Ganguly, J. Panda, Molecular structure, Hirshfeld surface analysis, theoretical investigations and nonlinear optical properties of a novel crystalline chalcone derivative: (E)-1-(5-bromothiophen-2-yl)-3-(p-tolyl)prop-2-en-1-one, J. Mol. Struct. 1161 (2018) 9–17.
[49] S.C. Jeyaseelan, A. Milton Franklin Benial, Quantum chemical, spectroscopic investigations, molecular docking and cytotoxic evaluation of 1-Methyl-indole-3-carboxaldehyde, Chem. Data Collect. 33 (2021) 100698.
[50] Christophe Morell, Andre´ Grand, Alejandro Toro-Labbe, New dual descriptor for chemical reactivity, J. Phys. Chem. 109 (2005) 205–212.
[51] M. Hagar, Hoda A. Ahmed, G. Aljohani, O.A. Alhaddad, Investigation of some antiviral *N*-Heterocycles as COVID 19 drug: molecular docking and DFT calculations, Int. J. Mol. Sci. 21 (2020) 3922.
[52] M. Ahmad, A. Dwivedy, R. Mariadasse, S. Tiwari, D. sikhaKar, J. Jeyakanthan, B.K. Biswal, Prediction of small molecule inhibitors targeting the severe acute respiratory syndrome Coronavirus-2 RNA-dependent RNA polymerase, ACS Omega 5 (2020) 18356–18366.
[53] P. Chowdhury, P. Pathak, Neuroprotective immunity by essential nutrient "Choline" for the prevention of SARS CoV2 infections: An in silico study by molecular dynamics approach. Chem. Phys. Lett. 761 (2020) 138057.
[54] P. Procacci, M. Macchiagodena, M. Pagliai, G. Guarnieri, F. Iannone, Interaction of hydroxychloroquine with SARS-CoV2 functional proteins using all-atoms non-equilibrium alchemical simulations, Chem. Commun. 56 (2020) 8854.
[55] M. Macchiagodena, M. Pagliai, P. Procacci, Identification of potential binders of the main protease 3CL ^{pro} of the COVID-19 via structure-based ligand design and molecular modeling, Chem. Phys. Lett. 750 (2020) 137489.
[56] S. Kumar, B. Singh, P. Kumari, P.V. Kumar, G. Agnihotri, S. Khan, T.K. Beuria, G.H. Syed, A. Dixit, Identification of multipotent drugs for COVID-19 therapeutics with the evaluation of their SARS-CoV2 inhibitory activity, Comput. Struct. Biotechnol. J. 19 (2021) 1998–2017.
[57] Sk. Abdul Amin, S. Banerjee, K. Ghosh, S. Gayen, T. Jha, Protease targeted COVID-19 drug discovery and its challenges: Insight into viral main protease (Mpro) and papain-like protease (PLpro) inhibitors, Bioorg. Med. Chem. (2020) 115860.
[58] The PyMOL (1.7.4.5 Edu) Molecular Graphics System, Schrodinger, LLC. Version 1.7.4.5.